Analytical description of the size effect on pyroelectric and electrocaloric properties of ferroelectric nanoparticles

Anna N. Morozovska,[1,2,*] Eugene A. Eliseev,[3] Maya D. Glinchuk,[3] Hanna V. Shevliakova,[4] George S. Svechnikov,[4] Maxim V. Silibin,[5,6,7] Artem V. Sysa,[8] Andrii D. Yaremkevich,[1] Nicholas V. Morozovsky,[1] and Vladimir V. Shvartsman[9,†]

[1]*Institute of Physics, National Academy of Sciences of Ukraine, 46, pr. Nauky, 03028 Kyiv, Ukraine*

[2]*Bogolyubov Institute for Theoretical Physics, National Academy of Sciences of Ukraine, 14-b Metrolohichna str. 03680 Kyiv, Ukraine*

[3]*Institute for Problems of Materials Science, National Academy of Sciences of Ukraine, Krjijanovskogo 3, 03142 Kyiv, Ukraine*

[4]*Department of Microelectronics, National Technical University of Ukraine "Igor Sikorsky Kyiv Polytechnic Institute," 03056 Kyiv, Ukraine*

[5]*National Research University of Electronic Technology, 124498 Zelenograd, Moscow, Russia*

[6]*Institute for Bionic Technologies and Engineering, I. M. Sechenov First Moscow State Medical University, 119991 Moscow, Russia*

[7]*Scientific-Practical Materials Research Centre of NAS of Belarus, 220072 Minsk, Belarus*

[8]*Research and Manufacturing Complex Technology Center "MIET," 124498 Zelenograd, Moscow, Russia*

[9]*Institute for Materials Science and Center for Nanointegration Duisburg-Essen (CENIDE), University of Duisburg-Essen, 45141, Essen, Germany*

(Received 10 June 2019; published 17 October 2019)

Using Landau-Ginzburg-Devonshire theory and effective medium approximation, we analytically calculate typical dependences of the pyroelectric and electrocaloric coefficients on external electric field, temperature, and radius of spherical single-domain ferroelectric nanoparticles. The considered physical model corresponds to the nanocomposite with a small fraction of ferroelectric nanoparticles. Within the framework of the analytical model, we establish how the size changes determine the temperature and field behavior of pyroelectric and electrocaloric coefficients on the example of $BaTiO_3$ nanoparticles covered by a semiconducting shell and placed in a dielectric polymer. We show that by changing the particle size one can induce maxima of the pyroelectric coefficient and electrocaloric temperature variation, control their width and height. Obtained analytical expressions allow selecting the interval of particle sizes, voltage, and/or temperature for which the pyroelectric energy conversion and electrocaloric coefficient are optimal for applications. The observed size effect opens the possibility to control pyroelectric and electrocaloric properties of ferroelectric nanocomposites that can be important for their advanced applications in energy convertors and cooling systems.

DOI: 10.1103/PhysRevMaterials.3.104414

I. INTRODUCTION

Nanosized ferroelectrics attract permanent attention of researchers as unique model objects for fundamental studies of polar surface properties, various screening mechanisms of spontaneous polarization by free carriers, and possible emergence of versatile multidomain states [1–6]. This fully applies to ferroelectric nanoparticles, for which effective procedures of synthesis and methods of polar properties control have been developed. Classical examples are the experimental results of Yadlovker and Berger [7,8], who revealed the ferroelectricity enhancement in Rochelle salt potassium nitrite nanorods. Frey and Payne [9], Zhao *et al.* [10], Drobnich *et al.* [11], Erdem *et al.* [12], Shen *et al.* [13], and Golovina *et al.* [14] demonstrated the possibility to control phase transition temperatures and other features of $BaTiO_3$, $Sn_2P_2S_6$, $PbTiO_3$, $SrBi_2Ta_2O_9$, and $KTa_{1-x}Nb_xO_3$ nanopowders and nanoceramics by finite-size effects. However, the ferroelectric nanoparticles still contain many challenges for technology [15] and theory [16].

The continuum phenomenological Landau-Ginzburg-Devonshire (LGD) approach combined with the electrostatic equations allows establishing the physical origins of the anomalies in the polar and dielectric properties of ferroelectric nanoparticles and predicts changes of their phase diagrams when the particle size decreases. For instance, using the LGD approach Perriat *et al.* [17], Huang *et al.* [18], Glinchuk *et al.* [19], Ma [20], Khist *et al.* [21], Wang *et al.* [22,23], Eliseev *et al.* [24,25], and Morozovska *et al.* [26–28], showed that the transition temperatures, the degree of spontaneous polar ordering in spherical, ellipsoidal, and cylindrical ferroelectric nanoparticles of size of 4–100 nm are conditioned by various physical mechanisms, such as surface tension, correlation effect, depolarization field originated from the incomplete screening of spontaneous polarization, flexoelectricity, electrostriction and Vegard-type chemical pressure.

Electrocaloric (ECE) and pyroelectric (PEE) effects that are inherent to ferroelectrics are the subjects of intensive experimental and theoretical studies [29–31]. Electrocaloric (EC) and pyroelectric (PE) properties of ferroelectrics at ferroelectric-antiferroelectric phase boundaries [32], ferroelectric thin films [33–36], multilayers [37–39], and other low-dimensional materials [40] can be very different from those of single crystals [41].

*Corresponding author: anna.n.morozovska@gmail.com

†Corresponding author: vladimir.shvartsman@uni-due.de

It is known [42,43] that the polar materials in adiabatic conditions are characterized by the PEE (charge or electric field generation under temperature change) and by the inverse ECE (temperature change under application or removal of an electric field). The vivid manifestation of PEE and ECE in ferroelectrics is a consequence of the strong temperature dependence of the spontaneous polarization [44–46], especially in the vicinity of phase transitions [47,48], or near the morphotropic phase boundary [49]. This property is the basis for the widespread applications of ferroelectric materials for pyroelectric detectors and energy converters, as well as for realizing their potentiality in modern electrocaloric converters [50–52].

At present, ECE and PEE in ferroelectric crystals, ceramics and polymers, thin films and multilayer structures are the objects of intensive theoretical, experimental, and applied studies. Nevertheless, ECE and PEE in ferroelectric nanoparticles are relatively poor studied. The possible reason is the strong influence of size effects via depolarization field [26] and polarization-strain coupling [22,27] on the polarization distribution, ferroelectric transition temperature, dielectric, PE, and EC properties. There are only few studies directed on the elucidation of the features of the PEE and ECE in nanowires, nanotubes [53–56], and spherical nanoparticles [57]. Moreover, the analytical description of ECE and PEE in ferroelectric nanoparticles and their nanocomposites, allowing for depolarization and incomplete screening effect, is still missing.

Using the LGD theory and effective medium approximation, this work analyzes typical dependences of the polarization, dielectric permittivity, PE and EC coefficients on external electric field, temperature, and radius for spherical ferroelectric nanoparticles covered by a semiconducting shell and placed in a dielectric medium. The considered physical model corresponds to a nanocomposite "nanoparticles-matrix" with a small fraction (less than 10%) of the ferroelectric nanoparticles.

The manuscript has the following structure. Problem statement, containing free energy, and basic equations with boundary conditions, is formulated in Sec. II. Section III introduces approximate analytical expressions for the transition temperature, EC temperature change, heat capacity, and related physical quantities. Size effects of ECE and PEE are analyzed in Sec. VI by the example of $BaTiO_3$ nanoparticles. Section V presents analysis of the size effect on the PE and EC energy conversion. Section VI contains conclusive remarks. Calculation details of the transition temperature, PEE and ECE, and auxiliary figures are presented in Ref. [58], Appendixes A, B, C, and D, respectively.

II. PROBLEM STATEMENT

Let us consider a spherical ferroelectric nanoparticle of radius R covered by a semiconducting shell of thickness Λ. The particle is placed in a dielectric medium (polymer, gas, liquid, air or vacuum) with an effective isotropic dielectric permittivity ε_e (Fig. 1).

A nanoparticle in a ferroelectric phase has a one-component spontaneous polarization $P_3(\mathbf{r})$ directed along the crystallographic axis 3. The dependence of other electric

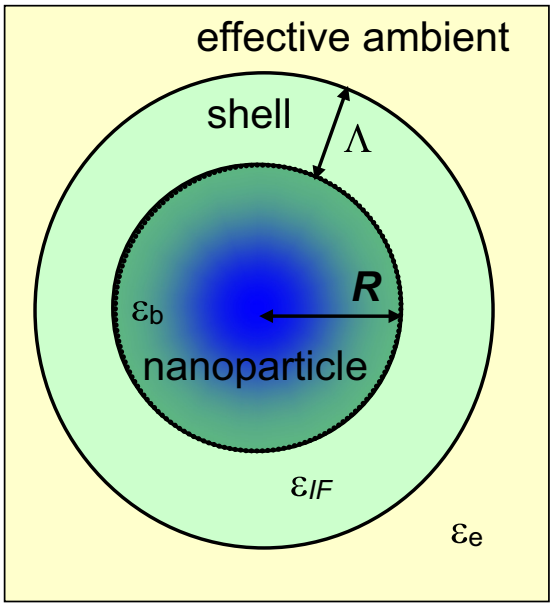

FIG. 1. A spherical ferroelectric nanoparticle (core) covered by a semiconducting layer (shell) and placed in a paraelectric or dielectric medium.

polarization components on the inner electric field $E_\mathbf{i}$ is linear, $P_i = \varepsilon_0(\varepsilon_b - 1)E_i$, where $i = 1$ and 2, ε_b is an isotropic relative permittivity of background [59], and ε_0 is the universal dielectric constant. Since the ferroelectric polarization component $P_3(\mathbf{r})$ contains both background and soft mode contributions, electric displacement vector has the form $\mathbf{D} = \varepsilon_0\varepsilon_b\mathbf{E} + \mathbf{P}$ inside the particle. Outside the particle $\mathbf{D} = \varepsilon_0\varepsilon_e\mathbf{E}$. The electric field components E_i depend on the electric potential φ as $E_i = -\partial\varphi/\partial x_i$. The potential φ satisfies the Poisson equation inside the particle and the Laplace equation outside it:

$$\varepsilon_0\varepsilon_b\left(\frac{\partial^2}{\partial x_1^2} + \frac{\partial^2}{\partial x_2^2} + \frac{\partial^2}{\partial x_3^2}\right)\varphi = \begin{cases} \frac{\partial P_3}{\partial x_3}, & r < R, \\ 0, & r > R \end{cases}. \tag{1a}$$

Equations (1a) are supplemented by the conditions of potential continuity at the particle surface, $(\varphi_{\text{ext}} - \varphi_{\text{int}})|_{r=R} = 0$ and field homogeneity at infinity, $\varphi_{\text{ext}}|_{r\to\infty} = -x_3E_{\text{ext}}$. Here, E_{ext} is the external electric field far from the particle. The boundary condition for the normal components of the electric displacements is $(\mathbf{n}(\mathbf{D}_{\text{ext}} - \mathbf{D}_{\text{int}}) + \sigma_S)|_{r=R} = 0$. The "effective" surface charge density σ_S is introduced to model realistic screening conditions of the spontaneous polarization. The polarization is incompletely screened at the ferroelectric particle surface and the screening degree depends on its ambient medium (dielectric, inert or chemically active gases, liquids, semiconductor or imperfect electrode cover). Several theoretical studies [21,25,28] use the linear dependence of the charge density σ_S on the electric potential excess at the surface of the nanoparticle, $\delta\varphi = \varphi_{\text{int}}|_{r=R} - \varphi_{\text{ext}}|_{r\to\infty}$:

$$\sigma_S[\varphi] \approx -\varepsilon_0\varepsilon_{\text{IF}}\frac{\delta\varphi}{\Lambda}, \tag{1b}$$

where an "effective" screening length Λ [28] and the interfacial dielectric permittivity ε_{IF} are introduced.

It should be noted that the expression (1b) is approximate because it includes an "effective" screening charge, while the real space charge is distributed in a ultrathin layer near the interface [60] or imperfect electrodes with nonzero screening length [61]. Stengel *et al.* [62,63] introduced the concept of the interfacial capacitance $C_{\rm IF}$ for the Λ description. Actually, $C_{\rm IF} = \varepsilon_0\varepsilon_{\rm IF}S/\Lambda$ (in a flat capacitor approximation) allows to justify the Eq. (1b), because the product $C_{\rm IF}\varphi|_{r=R}$ is the total value of the interfacial space charge, $q = \sigma_S S$, and therefore $\sigma_S = \frac{C_{\rm IF}\varphi|_{r=R}}{S} \approx -\varepsilon_0\varepsilon_{\rm IF}\frac{\varphi|_{r=R}}{\Lambda}$.

To fulfill the inequality $R \gg \Lambda$, reliable estimations of the Λ value should be used. Following Wang *et al.* [64] and Tagantsev *et al.* [65], the effective screening length Λ (more rigorously, $\Lambda/\varepsilon_{\rm IF}$), should be much smaller than 1 Å (about 0.1 Å) in accordance with modern *ab initio* estimations [65,66]. One of the reasons why the "effective" $\Lambda/\varepsilon_{\rm IF}$ can be much smaller than the typical perovskite lattice constant $a \sim 0.5$ nm [65], is the high relative dielectric permittivity $\varepsilon_{\rm IF}$ in the double electric layer, which typically is more than 100.

Another important case (relevant to the nanoparticles suspension in chemically active gases or liquids) is the Stephenson-Highland (SH) ionic adsorption at the ferroelectric surface [67,68]. Within SH model the dependence of the surface charge density $\sigma_S[\varphi]$ on the electric potential excess $\delta\varphi$ at the free surface is controlled by the concentration of positive and negative surface charges in a self-consistent manner via Langmuir adsorption isotherms, as is shown in Refs. [6,28].

Since we would not like to be limited to a specific model, further we perform calculations for Λ changing in the range (0.1–10) nm, and keep $\varepsilon_{\rm IF} > 100$ to provide an effective screening of the nanoparticle spontaneous polarization.

LGD free energy functional G additively includes 2-4-6 Landau expansion on polarization powers $G_{\rm Landau}$, polarization gradient energy contribution $G_{\rm grad}$, electrostatic contribution $G_{\rm el}$, elastic, electrostriction, and flexoelectric contributions $G_{\rm es+flexo}$. Following Ref. [28], it has the form

$$G = G_{\rm Landau} + G_{\rm grad} + G_{\rm el} + G_{\rm es+flexo}, \tag{2a}$$

$$G_{\rm Landau} = \int_{|\vec{r}|<R} d^3r\left(\frac{\alpha}{2}P_3^2 + \frac{\beta}{4}P_3^4 + \frac{\gamma}{6}P_3^6\right), \tag{2b}$$

$$G_{\rm grad} = \int_{|\vec{r}|<R} d^3r\left\{\frac{g_{11}}{2}\left(\frac{\partial P_3}{\partial x_3}\right)^2 + \frac{g_{44}}{2}\left[\left(\frac{\partial P_3}{\partial x_2}\right)^2 + \left(\frac{\partial P_3}{\partial x_1}\right)^2\right]\right\}, \tag{2c}$$

$$G_{\rm el} = -\int_{|\vec{r}|<R} d^3r\left(P_3E_3 + \frac{\varepsilon_0\varepsilon_b}{2}E_iE_i\right) - \int_{|\vec{r}|=R} d^2r\frac{\sigma_S\varphi}{2} - \frac{\varepsilon_0\varepsilon_e}{2}\int_{|\vec{r}|>R} E_iE_i d^3r, \tag{2d}$$

$$G_{\rm es+flexo} = \int_{|\vec{r}|<R} d^3r\left(-\frac{s_{ijkl}}{2}\sigma_{ij}\sigma_{kl} - Q_{ij3}\sigma_{ij}P_3^2 - F_{ijk3}\left(\sigma_{ij}\frac{\partial P_3}{\partial x_k} - P_3\frac{\partial \sigma_{ij}}{\partial x_k}\right)\right). \tag{2e}$$

The coefficient α linearly depends on temperature T, $\alpha = \alpha_T(T - T_C)$, where T_C is the Curie temperature and α_T is the inverse Curie-Weiss constant. Coefficients β and γ can be temperature-dependent (e.g., for $BaTiO_3$), $\beta = \beta_T(T - T_\beta)$ and $\gamma = \gamma_T(T - T_\gamma)$. Coefficient β is positive in the case of a second-order ferroelectric phase transition (FEPT) of and is negative in the case of a first-order FEPT. The gradient coefficients g_{11} and g_{44} are positive and regarded as temperature independent. In Eq. (2e), σ_{ij} is the stress tensor.

We omit the explicit form of the $G_{\rm es+flexo}$ for simplicity; it is described in Refs. [69–71]. Since the values of the electrostriction and flexoelectric tensor components, Q_{ijkl} and F_{ijkl}, respectively, are unknown for many ferroelectrics, we performed numerical calculations with the coefficients varied in a physically reasonable range ($|F_{ijkl}| \leqslant 10^{11}$ m^3/C, $|Q_{ijkl}| \leqslant 0.1$ m^4/C^2). Numerical results for $BaTiO_3$ single-domain nanoparticles with sizes above the critical one proved the insignificant impact of electrostriction and flexoelectric coupling on their polar properties, since appeared elastic fields are negligibly small in this case, and are concentrated in the immediate vicinity of the surface for small extrapolation lengths. However, one should consider both couplings for the rigorous determination of the critical size corresponding to the phase transition between the polydomain ferroelectric and paraelectric states of the nanoparticle or thin film, because the inhomogeneous elastic field induced by domain walls can be significant in the case (see, e.g., Refs. [1,2,6,22–24,70,71]).

It should be noticed that phenomenological LGD theory (by its definition) uses the bulk coefficients for the description of bulk and spatially confined ferroelectric micro- and nanosystems. The conditions of the size-induced phase transition follow from the contribution of the strain and polarization gradients, and depolarization/screening effects (see, e.g., Table I in Ref. [27] and references therein). The quantitative applicability of LGD approach depends on the system sizes, each of which should be much larger that the lattice constant, that is about 0.4 nm for ferroelectric perovskites (see, e.g., Refs. [6,28] and references therein).

Allowing for the Khalatnikov mechanism of polarization relaxation, minimization of the free energy (2) with respect to the polarization $P(r_3)$ leads to the time-dependent LGD equation [28]

$$\Gamma\frac{\partial P_3}{\partial t} + \alpha_T(T - T_C^*)P_3 + \beta P_3^3 + \gamma P_3^5 - g_{44}\left(\frac{\partial^2}{\partial x_1^2} + \frac{\partial^2}{\partial x_2^2}\right)P_3 - g_{11}\frac{\partial^2 P_3}{\partial x_3^2} = E_3. \tag{3a}$$

The Khalatnikov kinetic coefficient Γ determines the relaxation time of the polarization $\tau_K = \Gamma/|\alpha|$ that typically varies in the range $10^{-11} - 10^{-13}$ s far from FEPT. T_C^* is the Curie temperature renormalized by the surface stress [20,26]. The boundary condition for the polarization at the spherical surface $r = R$ is natural, $\partial\vec{P}_3/\partial\mathbf{n}|_{\rm r=R} = 0$, $\mathbf{n}$ is the outer normal to the surface. Below we also assume that the external field is $E_{\rm ext} = E_0\sin(\omega t)$.

The dynamic dielectric susceptibility defined as $\chi_{33} = \frac{\partial P_3}{\partial E_3}$ obeys the equation

$$\Gamma\frac{\partial \chi_{33}}{\partial t} + \left[\alpha_T(T - T_C^*) + 3\beta P_3^2 + 5\gamma P_3^4\right]\chi_{33} - g_{44}\left(\frac{\partial^2}{\partial x_1^2} + \frac{\partial^2}{\partial x_2^2}\right)\chi_{33} - g_{11}\frac{\partial^2\chi_{33}}{\partial x_3^2} = 1. \tag{3b}$$

TABLE I. LGD parameters for bulk ferroelectric $BaTiO_3$.[b]

ε_b	α_T (C^{-2} m J K^{-1})	$T_C(K)$	β (C^{-4} m^5 J)	γ (C^{-6} m^9 J)	$g_{11}(m^3/F)$	$g_{44}(m^3/F)$
7	6.68×10^5	381	$\beta_T(T-393) - 8.08 \times 10^8$ $\beta_T = 18.76 \times 10^6$	$\gamma_T(T-393) + 16.56 \times 10^9$ $\gamma_T = -33.12 \times 10^7$[a]	5.1×10^{-10}	0.2×10^{-10}

[a]These parameters are valid until $\gamma > 0$, i.e., for $T < 445$ K.
[b]$\rho = 6.02 \times 10^3$ kg/m^3, $C_p = 4.6 \times 10^2$J kg^{-1} K^{-1} at room temperature.

The dynamic PE coefficient defined as $\Pi_3 = -(\frac{\partial P_3}{\partial T})_E$ obeys the equation

$$\Gamma\frac{\partial \Pi_3}{\partial t} + \left[\alpha_T\left(T - T_C^*\right) + 3\beta P_3^2 + 5\gamma P_3^4\right]\Pi_3 - g_{44}\left(\frac{\partial^2}{\partial x_1^2} + \frac{\partial^2}{\partial x_2^2}\right)\Pi_3 - g_{11}\frac{\partial^2 \Pi_3}{\partial x_3^2} = \alpha_T P_3. \tag{3c}$$

The EC temperature change ΔT_{EC}, can be calculated from the expression:

$$\Delta T_{\mathrm{EC}} = -T\int_{E_1}^{E_2}\frac{1}{\rho C_P}\left(\frac{\partial P}{\partial T}\right)_E dE \cong T\int_{E_1}^{E_2}\frac{1}{\rho C_P}\Pi_3 dE, \tag{4a}$$

where ρ is the density, T is the ambient temperature, and C_p is the specific heat. For ferroics, the specific heat depends on polarization (and so on external field) and can be modeled as following [72]:

$$C_P = C_P^0 - T\frac{\partial^2 g}{\partial T^2}, \tag{4b}$$

where C_P^0 is the polarization-independent part of specific heat and g is the density of the LGD free energy (2). According to experiment, the specific heat usually has a jump at the second-order FEPT and has a maximum at the first-order FEPT, which height is about 10%–30% of the C_p value near T_C (see, e.g., Refs. [37,73]). Corresponding entropy change is given by expression $\Delta S = -\int_{E_1}^{E_2}(\frac{\partial P}{\partial T})_E dE$.

Finite element modeling (FEM) has been performed to find the solution of a coupled equations system (1)−(4) for $BaTiO_3$ nanoparticles placed in a polymer matrix, since such nanocomposites have been intensively studied for energy storage, PEE, and ECE applications [74–76]. We have chosen $BaTiO_3$ because it is a classical proper ferroelectric with a relatively high spontaneous polarization at room temperature, relatively low FEPT temperature and well-known material parameters. $BaTiO_3$ undergoes the first-order FEPT from the ferroelectric to paraelectric phase. The first-order FEPT adds additional interesting peculiarities of PE and EC properties, analyzed below, in comparison with the ferroelectric materials undergoing the second-order FEPT. Material parameters of $BaTiO_3$ were collected from Refs.[77–80] and references therein; they are listed in Table I of this paper and Table AI in Ref. [58].

FEM results are shown in Fig. 2, where we have taken into consideration the multiaxiality of $BaTiO_3$, electrostriction and flexoelectric couplings, and have used the free energy expansion with the material parameters from Table AI in Ref. [58]. Two sets of initial conditions were used for the polarization distributions, namely bi-domain and single-domain structures. The initial bidomain structure was transformed into a vortexlike structure with the polarization rotating to align parallel to the particle surface in order to minimize the depolarization electric field. As the result, the latter could not be reduced to zero, but its amplitude becomes significantly smaller [compare the scale in Fig. 2(a) with Fig. 2(b)].

It turned out that the vortexlike domain structure (as an electric toroidal multipole) is much less sensitive to a homogeneous external field than the single-domain state (electric dipole), unless the field reaches values significantly higher than the coercive field for a single-domain state. So, the polarization vortex presents less interest for pyroelectric applications, since it is electroneutral as a whole. For electrocaloric applications, where the polarization response to small external fields should be as high as possible, the vortex state also seems less favorable than the single-domain state. Actually, to change the toroidal moment of vortex polarization the curled electric field, $\vec{E}_{\mathrm{cur}} = \frac{1}{2}\vec{Q} \times \vec{r}$, originated from a quasistatic magnetic field, $\mathrm{rot}\vec{E}_{\mathrm{cur}} = -\frac{\partial}{\partial t}\vec{B}$, is required [54,56]. Corresponding vorticity vector $Q^3 10^{16}$ V/m^2 is very high [81].

However, the vortexlike domain structure is relatively sensitive to the screening conditions of ferroelectric polarization, namely, it occurs and becomes absolutely stable with increasing $\Lambda/\varepsilon_{\mathrm{IF}}$. Thus it makes sense using enough small values of $\Lambda/\varepsilon_{\mathrm{IF}}$ to keep the nanoparticle in a stable single-domain state. Below we consider $\Lambda/\varepsilon_{\mathrm{IF}} \ll 1$ nm proving the stable single-domain state of the nanoparticle.

Note that Chen and Fang [57] considered ECE in $BaTiO_3$ nanoparticle within core-shell model. Unfortunately, the depolarization effects, which are inevitable in the case of zero polarization at the particle surface considered in Ref. [57], were completely neglected, and this fact does not allow us applying obtained results to real systems.

III. APPROXIMATE ANALYTICAL SOLUTION

Phase diagrams of spherical ferroelectric nanoparticles covered by a screening charge layer have several phases, namely, paraelectric phase, single-domain ferroelectric phase and polydomain ferroelectric phase including various domain morphologies [28]. Free energy with renormalized coefficients has the form (see Appendix A in Ref. [58]):

$$g_R = \alpha_T[T - T_{\mathrm{cr}}(R,\Lambda)]\frac{P^2}{2} + \beta(T)\frac{P^4}{4} + \gamma(T)\frac{P^6}{6} - \eta P E_{\mathrm{ext}}, \tag{5a}$$

where E_{ext} is the external electric field and $\bar{P}_3 \equiv P$. Approximate expression for the nanoparticle transition temperature T_{cr} from the single-domain ferroelectric to paraelectric

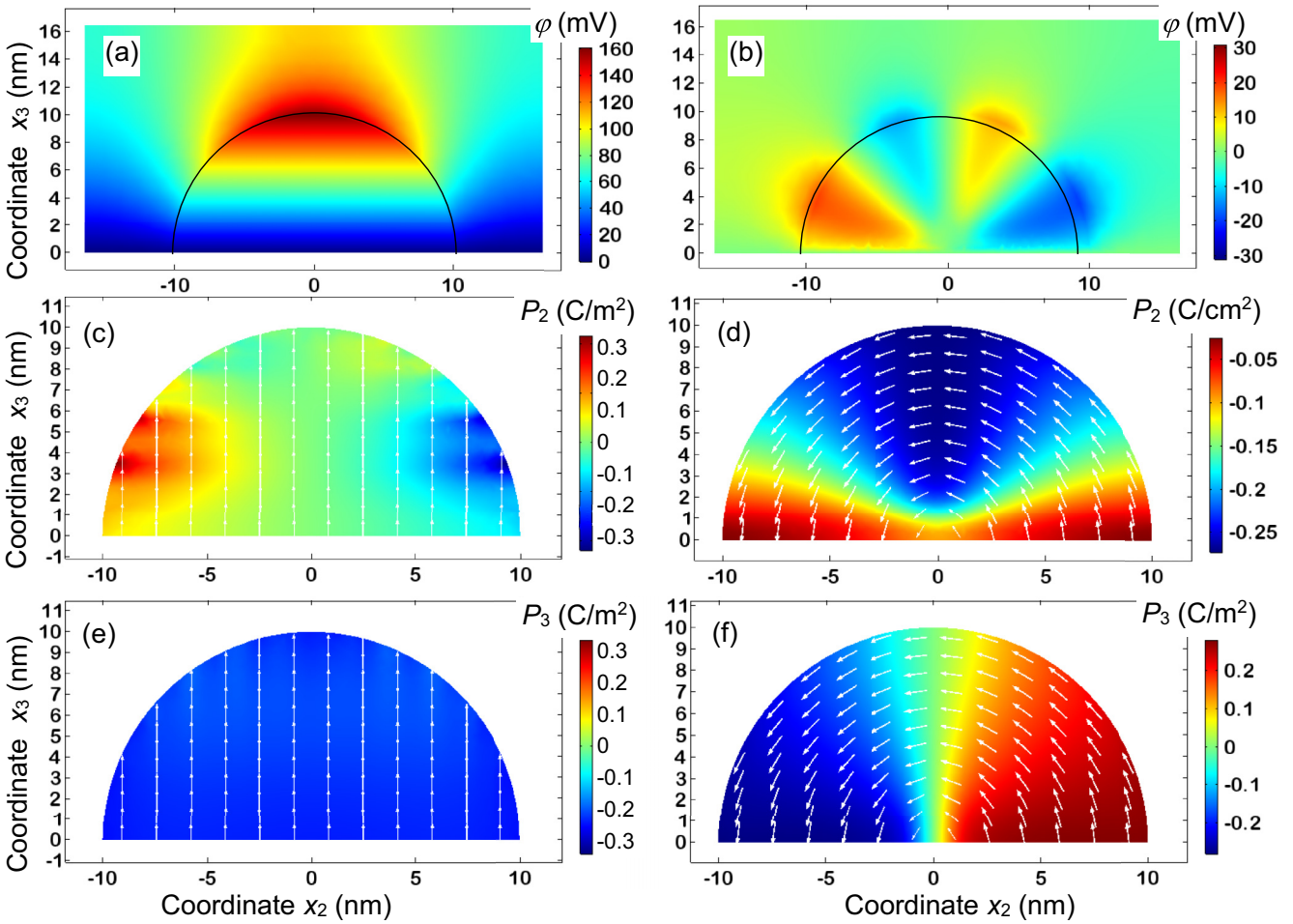

FIG. 2. Distribution of electrostatic potential [(a) and (b)], polarization components P_2 [(c) and (d)] and P_3 [(e) and (f)] in the cross-section $x_2 = 0$ of the $BaTiO_3$ nanoparticle with radius 10 nm. Two different states are shown, single domain [(a), (c), and (e)] and vortexlike structure [(b), (d), and (f)]. White arrows show polarization direction. Calculations were performed at $T = 293$ K, $\varepsilon_{IF} = 300$, $\Lambda = 2$ nm, $\varepsilon_e = 15$. $BaTiO_3$ parameters are listed in Table I for the left plots [(a), (c), and (e)] and in Table AI in Ref. [58] for the right plots [(b), (d), and (f)].

phase is

$$T_{cr}(R, \Lambda) = T_C^* - \frac{1}{\alpha_T \varepsilon_0 [\varepsilon_b + 2\varepsilon_e + \varepsilon_{IF}(R\Lambda)]}, \tag{5b}$$

Here the first term T_C^* is the Curie temperature renormalized by the surface stress. The second term originates from a depolarization field [28].

In Eq. (5a), we introduced the screening factor of the external field,

$$\eta(R, \Lambda) = \frac{3\varepsilon_e}{\varepsilon_b + 2\varepsilon_e + \varepsilon_{IF}(R/\Lambda)}. \tag{5c}$$

Derivation of Eqs. (5) is given in Appendix A in Ref. [58]. Note that Eqs. (5) are exact if the natural boundary conditions for polarization are imposed at the particle surface. The depolarization factor $\eta(R, \Lambda)$ in a definite sense determines peculiarities of size effects in spherical nanoparticles, because its form is the result of complex influence of geometry (shape), ambience (dependence of dielectric constants) and depolarization field defined by specific screening conditions contributing to the effective screening length ε_{IF}/Λ. The form and values of the depolarization factor can be very different for thin films and nanoparticles of different shape. The knowledge of η is required for quantitative understanding of the physical picture, while qualitatively it typically (but far not always) scales as $1/L$, where L is a characteristic size of the nanosystem.

Minimization of the free energy Eqs. (5) leads to the equation for the polarization $\alpha_T(T - T_{cr})P + \beta P^3 + \gamma P^5 = \eta E_{ext}$. Differentiation of the equation over external field and temperature leads to the equations $(\alpha_T(T - T_{cr}) + 3\beta P^2 + 5\gamma P^4)(\frac{dP}{dE_{ext}})_T = \eta$ and $(\frac{\partial P}{\partial T})_E[\alpha_T(T - T_{cr}) + 3\beta P^2 + 5\gamma P^4] = -\alpha_T P - \beta_T P^3 - \gamma_T P^5$, respectively. Using these equations, we derived analytical expressions for PE coefficient and EC temperature change:

$$\Pi(R, \Lambda) = \frac{\alpha_T P + \beta_T P^3 + \gamma_T P^5}{\alpha_T [T - T_{cr}(R, \Lambda)] + 3\beta P^2 + 5\gamma P^4}, \tag{6a}$$

$$\Delta T_{EC} = \frac{T}{\rho} \int_{E_1}^{E_2} \frac{\Pi(R, \Lambda, P(E))}{C_P} dE$$

$$= \frac{T}{\eta \rho} \int_{P_1}^{P_2} \frac{\alpha_T P + \beta_T P^3 + \gamma_T P^5}{C_P} dP$$

$$\approx \frac{T}{\eta\,\rho C_P}\left\{\frac{\alpha_T}{2}[P^2(E_2)-P^2(E_1)] + \frac{\beta_T}{4}[P^4(E_2)-P^4(E_1)]+\frac{\gamma_T}{6}[P^6(E_2)-P^6(E_1)]\right\} \tag{6b}$$

Approximate equality in the expression (6b) is valid for the case of a ferroelectric with the linearly temperature dependent LGD-expansion coefficients (e.g., for $BaTiO_3$), and for a negligibly weak field dependence of the specific heat that may be a rough approximation for vast majority of ferroelectric perovskites. More rigorously,

$$C_P \approx \begin{cases} C_P^0 + \frac{T\left(\alpha_T P+\beta_T P^3+\gamma_T P^5\right)^2}{\alpha_T(T-T_{\rm cr})+3\beta P^2+5\gamma P^4}, & T < T_\theta, \\ C_P^0, & T > T_\theta, \end{cases} \tag{7}$$

where $T_\theta = T_{\rm cr} + \frac{\beta^2}{4\gamma\alpha_T}$ is the maximal temperature of the ferroelectric phase metastability. Derivation of Eq. (7) utilizes Eq. (4b) and the fact that the g_R derivatives simplifies allowing for the equation $\alpha_T(T-T_{\rm cr})P+\beta P^3+\gamma P^5 = \eta E_{\rm ext}$ (see Appendix B in Ref. [58]). Following Landau theory, the dielectric susceptibility $\chi_E = \frac{1}{\alpha_T(T-T_{\rm cr})+3\beta P^2+5\gamma P^4}$ diverges at $T = T_\theta$ and $E_{\rm ext} = 0$, while the polarization is finite for the first-order phase transitions, leading to the divergence of the difference $\delta C_P = C_P - C_P^0$. In reality both the external electric field and critical fluctuations transform the divergence into a maximum that is typically ≈10%–30% in height of C_P (however there can be exceptions). Typically, the maximum shape cannot be described by a rigorous analytical expression, but semiempirically as $\chi_E = \frac{1}{\sqrt{\left(\alpha_T(T-T_{\rm cr})+3\beta P^2+5\gamma P^4\right)^2+\delta^2}}$, where the empirical parameter δ is small enough.

Since the polarization-dependent term $\frac{T\left(\alpha_T P+\beta_T P^3+\gamma_T P^5\right)^2}{\alpha_T(T-T_{\rm cr})+3\beta P^2+5\gamma P^4}$ is positive, it always increases C_P and so decreases the integrand expression in Eq. (6b). As a result, the approximate expression (6b) overestimates the ECE.

If the dimensionless parameter $\mu = \frac{T\alpha_T^3}{C_P^0\beta_T^2}\bar{\chi}_E$ is small, the first-order corrections to Eq. (6b) have the form

$$\Delta T_{\rm EC} \approx \frac{T}{\eta\,\rho C_P^0}\left(\frac{\alpha_T}{2}[P^2(E_2)-P^2(E_1)] + \frac{\beta_T(1-\mu)}{4}[P^4(E_2)-P^4(E_1)] + \frac{\gamma_T - 3\mu\alpha_T^{-1}\beta_T^2}{6}[P^6(E_2)-P^6(E_1)] + \ldots\right). \tag{8}$$

In the linear approximation, valid for weak enough external fields (i.e., for $E_{\rm ext}$ much lower than the coercive field), $P(E_{\rm ext}) \approx P(0) - \frac{\eta E_{\rm ext}}{2\alpha_T(T-T_{\rm cr})}$, and so $P^2(E_{\rm ext}) - P^2(0) \approx -\frac{\eta E_{\rm ext} P_S}{\alpha_T(T-T_{\rm cr})}$, where $P(0) \equiv \pm P_S$ is the nanoparticle spontaneous polarization. Within the approximation

$$\Delta T_{\rm EC}(E_{\rm ext}) \approx -\frac{T}{\rho C_P^0}\left(\alpha_T P_S + \beta_T P_S^3 + \gamma_T P_S^5\right)\frac{E_{\rm ext}}{2\alpha_T(T-T_{\rm cr})}, \tag{9}$$

and the nanoparticle spontaneous polarization is

$$P_S(R,\Lambda,T) = \sqrt{\frac{1}{2\gamma}\left[\sqrt{\beta^2+4\gamma\alpha_T(T_{\rm cr}(R,\Lambda)-T)}-\beta\right]}. \tag{10}$$

IV. SIZE EFFECT ON PYROELECTRIC AND ELECTROCALORIC PROPERTIES

Below we analyze the correlations between the nanoparticle polarization P, relative dielectric permittivity $\varepsilon_{\rm NP}$, PE coefficient Π, and EC temperature change $\Delta T_{\rm EC}(E)$ calculated for a periodic external electric field, $E_{\rm ext} = E_0\sin(\omega t)$, different temperature T, and nanoparticle radius R. The static dependences have been calculated under the absence of time derivative in the LGD-type equations (3) and setting $\omega = 0$ in the expression for the external field $E_{\rm ext} = E_0\sin(\omega t)$. By acting in this way not only stable, but also metastable and unstable solutions can be obtained. For example, the numerical solution of "dynamic" toy-model equation $\Gamma\frac{\partial P_3}{\partial t} + \alpha P_3 + \beta P_3^3 + \gamma P_3^5 = E_0$ at $\Gamma > 0$ converges to the stable solution only. Its static analog, $\alpha P_3 + \beta P_3^3 + \gamma P_3^5 = E_0$, as a fifth-order polynomial equation, can have five different roots, among which there is always a stable solution to which the dynamical numerical algorithm converges.

Despite that the use of direct or alternating electric voltage is not an established experimental method for measuring PEE (see, e.g., Refs. [43,83–85]), the pyroelectric energy conversion often involves the voltage application [82,84,86]. Concerning the electrocaloric measurements, both direct and alternating electric fields are applied, that allows obtaining valuable information about EC response and, especially, its field hysteresis, which requires electric field reversal (see, e.g., Refs. [29–39]). That is why below we plot and analyze both dynamic and static dependences of PE and EC responses whenever it is possible.

Figures 3–6 show typical dependences of P, $\varepsilon_{\rm NP}$, Π, and $\Delta T_{\rm EC}$ on $E_{\rm ext}$, T, and R for $BaTiO_3$ nanoparticles with parameters listed in Table I. All dependences are calculated for the relatively high interfacial permittivity $\varepsilon_{\rm IF} = 300$ (that is realistic for paraelectric shells), enough high effective screening length $\Lambda = 2$ nm, and ambient permittivity $\varepsilon_e = 15$ characteristic for a high-k dielectric matrix (e.g., widely used PVDF). We compared the "static" dependences (dashed curves), which include unstable and metastable regions, with thermodynamically stable "dynamic" dependences (solid curves) calculated for the external field frequency $\omega = 2\times 10^4\ {\rm s}^{-1}$. Note that temperature and size dependences P, $\varepsilon_{\rm NP}$, Π, and $\Delta T_{\rm EC}$ shown in Figs. 4–6 correspond to the "positive" branches of their hysteresis in Fig. 3(a).

Dependences of P, $\varepsilon_{\rm NP}$, Π, and $\Delta T_{\rm EC}$ on $E_{\rm ext}$ are shown in Figs. 3(a)–3(d), respectively. The dependences are

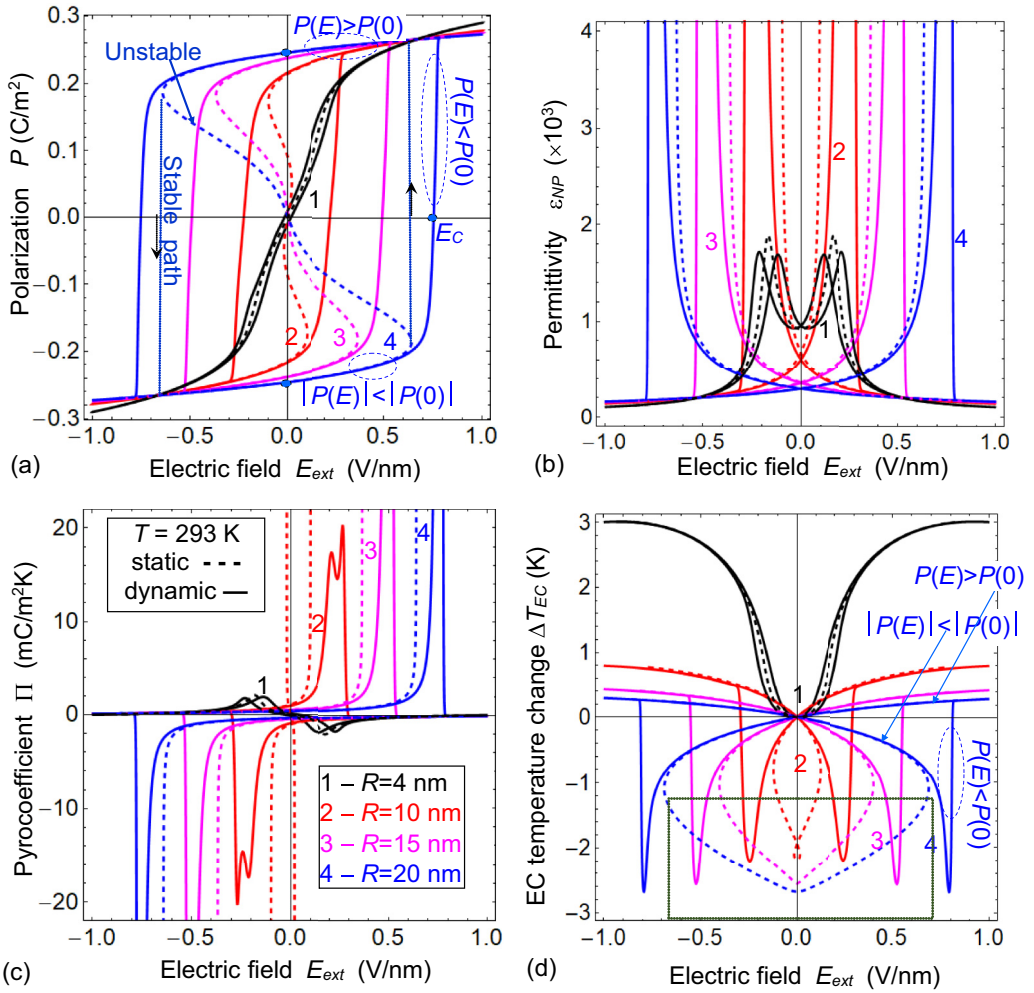

FIG. 3. Dependences of the polarization (a), relative dielectric permittivity (b), PE coefficient (c), and EC temperature change (d) on external electric field calculated for several radii $R = 4$, 10, 15, 20 nm of $BaTiO_3$ nanoparticle (curves 1–4), $T = 293$ K, $\varepsilon_{IF} = 300$, $\Lambda = 2$ nm, $\varepsilon_e = 15$, $\Gamma = 10^2$ SI units, and $\omega = 2 \times 10^4\ s^{-1}$ for solid curves. The static dependences ($\omega = 0$) including unstable regions are shown by dashed curves. Dotted vertical lines with arrows in plot (a) show stable paths. The unstable dependences are shown by dashed curves inside the dotted rectangle in plot (d). Dashed ellipses in (a) and (d) indicate the regions, where $|P(E_{ext})| > |P(0)|$ or $|P(E_{ext})| < |P(0)|$, respectively. $BaTiO_3$ parameters are listed in Table I, its density $\rho = 6.02 \times 10^3$ kg/m^3 and specific heat $C_p = 4.6 \times 10^2$ J|kg^{-1}|K^{-1} at room temperature.

calculated for several nanoparticle radii R (curves 1 – 4) at room temperature. The ferroelectric hysteresis loop ($P(E_{ext})$) is narrow for the smallest particle ($R = 4$ nm), then it expands and becomes significantly wider (i.e., the coercive field E_C increases) with the increasing particle radius [compare solid curves 1–4 in Fig. 3(a)]. Note that the appearance of a very narrow hysteresis loop at $R = 4$ nm is a purely dynamic effect observed at nonzero frequency ω. Actually, the static dashed black curve calculated for $R = 4$ nm does not contain any unstable S-shaped region. Other static curves calculated for $R > 5$ nm contain the unstable S-shaped region corresponding to the bistable states of the ferroelectric polarization. All curves and loops in Fig. 3(a) show the behavior typical for the ferroelectric nanoparticles undergoing the first-order FEPT to a paraelectric phase with R decrease (i.e., the size-induced phase transition). From Eq. (5b) the critical radius R_{cr} of the size-induced transition is given by expression,

$$R_{cr}(T, \Lambda) = \Lambda\left(\frac{1}{\alpha_T \varepsilon_0 \varepsilon_{IF}(T_C^* - T)} - \frac{\varepsilon_b + 2\varepsilon_e}{\varepsilon_{IF}}\right). \quad (11)$$

From Eq. (11) the critical size is about 8 nm at 293 K and $E_0 = 0$, and so the particle with $R = 4$ nm is paraelectric, and other with $R = 10 - 20$ nm are ferroelectric at room temperature.

Correlating with Fig. 3(a), Figs. 3(b) and 3(c) illustrate the characteristic features (maximum, sharp double maximum, or divergence) of ε_{NP} and Π emerging in the vicinity of the coercive field that value increases with the R increase. Maxima correspond to nonzero frequency $\omega > 0$, and divergences are for $\omega = 0$. The "unphysical" values of negative permittivity corresponding to the unstable S-shaped regions in Fig. 3(a) (dashed curves) are not shown in Fig. 3(b).

The dependences $\Delta T_{EC}(E_{ext})$ calculated at $\omega \neq 0$ [solid curves in Fig. 3(d)] correlate with the dependences $\varepsilon_{NP}(E_{ext})$ [solid curves in Fig. 3(b)], but have several distinctive features. For the smallest "paraelectric" particles ($R \leqslant 4$ nm) the $\Delta T_{EC}(E_{ext})$ static dependences (dashed curves) and very narrow dynamic loops (solid curves) have a vase shape (without maximums). The ΔT_{EC} value monotonically increases and then saturates with E_{ext} increasing [solid curve 1 in Fig. 3(d)].

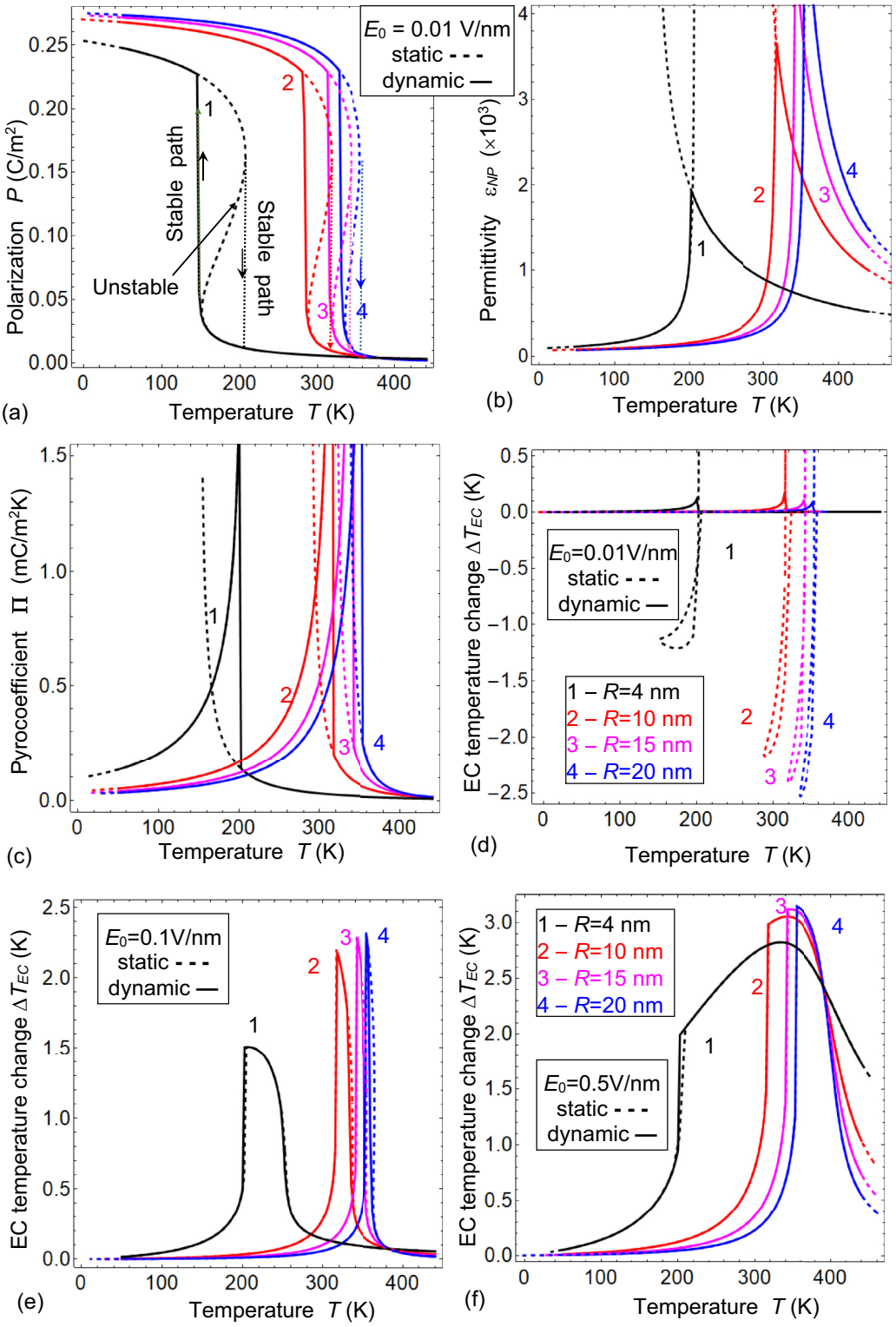

FIG. 4. Temperature dependences of polarization (a), relative dielectric permittivity (b), PE coefficient (c), and EC temperature change [(d)−(f)] calculated for several radii of $BaTiO_3$ nanoparticle $R = 4$, 10, 15, and 20 nm (curves 1–4) and external electric field amplitude $E_0 = 0.01$ [(a)–(d)], 0.1 (e), and 0.5 V/nm (f). The field frequency $\omega = 2 \times 10^4\ s^{-1}$ for solid curves, and $\omega = 0$ for dashed curves, which include unstable regions. Dotted vertical lines with arrows show stable paths. Other parameters are the same as in Fig. 3.

In the "paraelectric" phase, ECE is positive ("heating" effect). It should be mentioned, that such behavior correlates with quadratic field dependence of the electrocaloric effect in a bulk paraelectric [82].

The EC temperature change shown in Fig. 3(d) is positive for the smallest particle, but becomes bipolar with the increasing particle size. This happens because the smallest particle ($R = 4$ nm) is paraelectric, and its polarization is

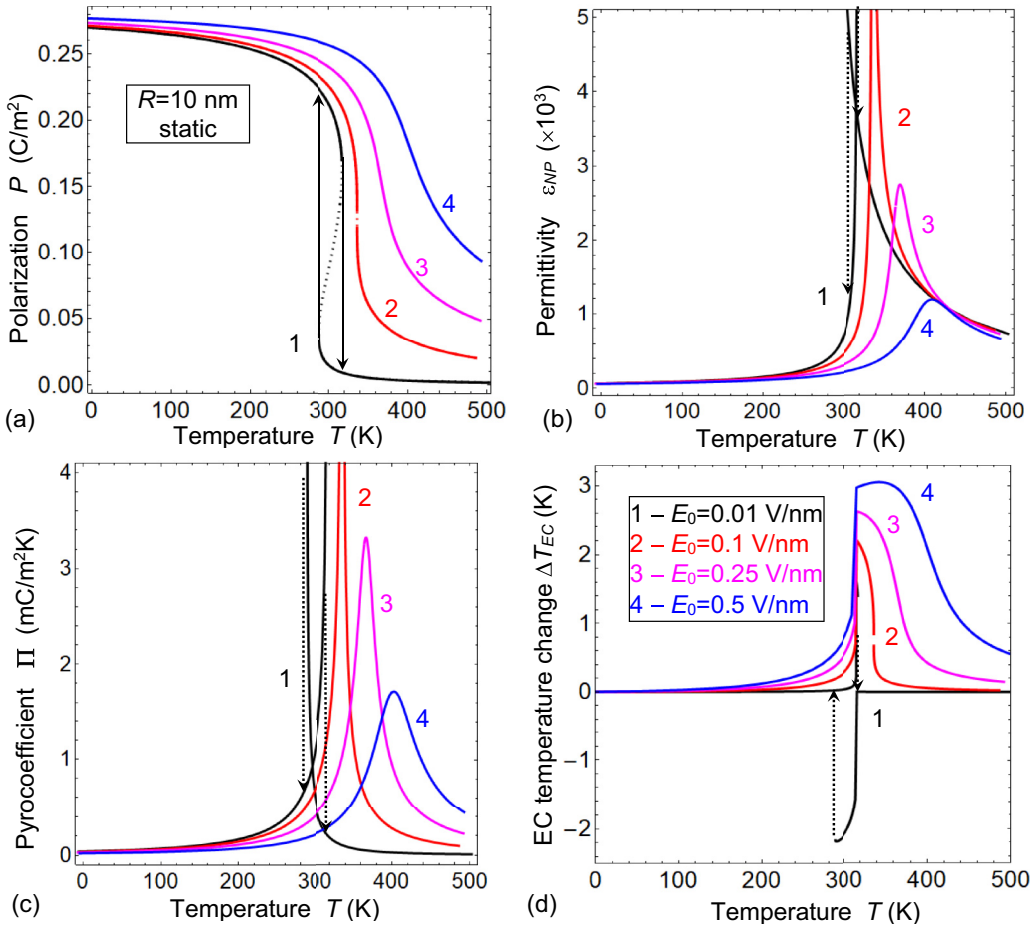

FIG. 5. Static temperature dependences of the $BaTiO_3$ nanoparticle polarization (a), relative dielectric permittivity (b), PE coefficient (c), and EC temperature change (d) calculated for $BaTiO_3$ nanoparticle with radius of $R = 10$ nm and different external field $E_0 = 0.01$, 0.1, 0.25, and 0.5 V/nm (curves 1–4). Other parameters are the same as in Fig. 3.

induced by external field only. Actually, the EC temperature change of a paraelectric particle is always positive, since $\Delta T_{\rm EC}(E_{\rm ext}) \approx \frac{T}{\eta \rho C_P}\frac{\alpha_T}{2}[P^2(E_{\rm ext}) - P^2(0)] > 0$ if $|P(E_{\rm ext})| > |P(0)|$ at $|E_{\rm ext}| > 0$ [see Eq. (6b)]. When the particle becomes ferroelectric with R increased above the critical size (e.g., for $R \geqslant 10$nm), the ferroelectric polarization hysteresis exists [see Fig. 3(a)]. It is seen from the polarization hysteresis loops [Fig. 3(a)] that both inequalities $|P(E_{\rm ext})| > |P(0)|$ and $|P(E_{\rm ext})| < |P(0)|$ are valid due to the polarization bistablity in the hysteresis range at $0 \leqslant |E_{\rm ext}| < E_c$ (E_c is a coercive field). Consequently E-field dependence of EC temperature change is bistable in the range $0 \leqslant |E_{\rm ext}| < E_c$, where both positive and negative "branches" exist, and it changes its sign to positive at $|E_{\rm ext}| = E_c$ [see solid red, magenta and blue curves in Fig. 3(d)]. The ECE changes its sign to negative ("cooling" effect) when the electric field becomes antiparallel to the polarization direction. In this case the applied electric field destabilizes the polarized state and therefore increases the entropy. This is the "physical origin" of the negative ECE. As soon as the polarization is switched along the electric field at $|E_{\rm ext}| = E_c$, the ECE again changes its sign to positive. In the ferroelectric phase (for $R \geqslant 10$ nm) ECE is relatively small with the exception of the coercive field vicinity, where it reaches minus 2–3 K. These ECE maxima sharpness and their magnitude increases with the increasing particle radius. The static $\Delta T_{\rm EC}(E_{\rm ext})$ dependences [Fig. 3(d), dashed curves 2–4] almost coincide with dynamic those [Fig. 3(d), solid curves 2–4], except for the instability region marked by a dotted rectangle [see Fig. 3(d), bottom].

As can be seen from the Figs. 3(c) and 3(d), one can induce the appearance, control the width, magnitude, and sign of $\Pi(E_{\rm ext})$ and $\Delta T_{\rm EC}(E_{\rm ext})$ maxima by changing the particle size, as well as tune the field interval within which PEE and ECE are maximal.

Temperature dependences $P(T)$, $\varepsilon_{\rm NP}(T)$, $\Pi(T)$, and $\Delta T_{\rm EC}(T)$, calculated for the several radii of nanoparticles and a relatively small amplitude of external field ($E_0 = 0.01$ V/nm) in the vicinity of the FEPT region, are shown in Figs. 4(a)–4(d). The amplitude E_0 is well below the thermodynamic coercive field of polarization reversal in our case (0.2–0.8 V/nm) Fig. 3(a). The temperature "hysteresis", defined as the interval between the solid and dotted vertical lines, is the widest for the smallest R and narrows when the particle radius increases [compare solid and dashed curves 1–4 in Fig. 4(a)]. The origin of the hysteresis is thermodynamic bistability, therefore it disappears at bigger E_0 and/or for higher ω. The hysteresis position corresponds to the vicinity of the transition temperature $T_{\rm cr}$, which is particle size

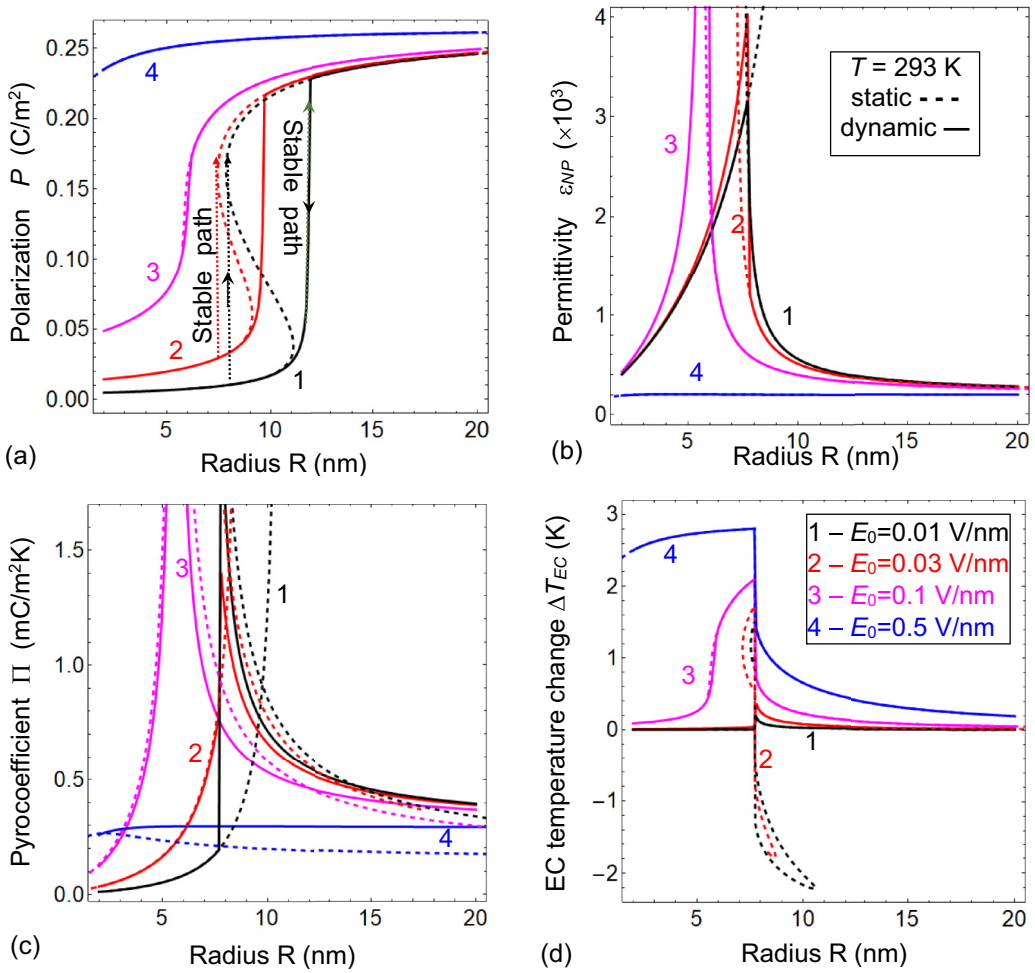

FIG. 6. Size dependences of the $BaTiO_3$ nanoparticle polarization (a), relative dielectric permittivity (b), PE coefficient (c), and EC temperature change (d) calculated at $T = 293$ K for several amplitudes of external field $E_0 = 0.01$, 0.03, 0.1, and 0.5 V/nm (curves 1–4), frequency $\omega = 2 \times 10^4\ s^{-1}$ (solid curves) and $\omega = 0$ (dashed curves). Other parameters are the same as in Fig. 3.

dependent and goes up with increasing R, in agreement with Eq. (5b).

In fact, all static dependences in Fig. 4 (dashed curves 1–4) contain the unstable S-shaped regions, which width decreases with the increasing particle size. The dependences $P(T)$ in Fig. 4(a) show the behavior typical for the ferroelectric nanoparticle undergoing the first-order FEPT below T_{cr}. Correlating with Fig. 4(a), Figs. 4(b) and 4(c) show typical sharp maxima at $\omega > 0$ on $\varepsilon_{NP}(T)$ and $\Pi(T)$ or their divergence for $\omega = 0$ emerging at $T_{cr}(R)$. The "unphysical" regions of the negative permittivity, corresponding to the unstable "inverse S"-shaped regions at the dashed curves in Fig. 4(a) are not shown in Fig. 4(b).

Temperature dependences of EC temperature change $\Delta T_{EC}(T)$, calculated at frequency $\omega \neq 0$, $R = 4 - 20$ nm nm and $E_0 = 0.01 - 0.5$ V/nm are shown by solid curves in Figs. 4(d)–4(f). They reveal several distinct features. Correlating with the $P(T)$ behavior at FEPT [shown in Fig. 4(a)], maximal ΔT_{EC} is located around T_{cr}. For $E_0 = 0.01$ V/nm, $\Delta T_{EC}(T)$ is rather small and positive in the region of $P(T)$ hysteresis for all R [see solid curves 1–4 in Fig. 4(d)]. The maximal value of ΔT_{EC} increases by 2–3 K and the maximum width strongly increases (up to 50–300 K) with increasing E_0 value for all considered R [see solid curves 1–4 in Figs. 4(e) and 4(f)]. However, the width of ΔT_{EC} peak significantly decreases with the increasing R [see solid curves 1–4 in Figs. 4(e) and 4(f)].

Note that at $E_0 \ll 0.1$ V/nm the static dependences contain regions of the negative ECE [see negative parts of dashed curves 1–4 in Fig. 4(d)] corresponding to the unstable S-shaped regions on polarization curves in Fig. 4(a).

The dependences $\Delta T_{EC}(T)$ calculated for rather high amplitude $E_0 = 0.5$ V/nm are shown in Fig. 4(f) and reveal several distinctive features in comparison with Figs. 4(d) and 4(e). First, for all particle sizes, the maximum of $\Delta T_{EC}(T)$ lies definitely below the peak of the dielectric permittivity. Second, the temperature range of the maximal ΔT_{EC} narrows and shifts to higher temperatures when the particle radius increases due to FEPT sharpening and the shift of T_{cr}. Note that even at the strong fields we still can control the temperature range and width of the maximal PEE and ECE by changing the particle size (see also Appendix C in Ref. [58]).

As can be seen from the Figs. 4(c) and 4(f), one can control the width and height of $\Pi(T)$ and $\Delta T_{EC}(T)$ peaks by changing the particle size and amplitude of E_{ext}, as well as select the temperature interval where $\Pi(T)$ and $\Delta T_{EC}(T)$ are maximal.

The static temperature dependences $P(T)$, $\varepsilon_{NP}(T)$, $\Pi(T)$, and $\Delta T_{EC}(T)$ calculated for several values of the constant external field $E_{ext} = E_0$ and $R = 10$ nm are shown in Figs. 5(a)–5(d). The temperature hysteresis of $P(T)$ existing for small E_0 [shown by black dotted lines in Fig. 5(a)] disappears, and the dependence $P(T)$ becomes significantly smeared with E_0 increasing above a critical field E_{cr} that is about 0.1 V/nm for $R = 10$ nm [compare solid curves 1–4 in Fig. 5(a)]. Correlating with Fig. 5(a), Figs. 5(b)–5(c) show rather asymmetric maxima of the $\varepsilon_{NP}(T)$ and $\Pi(T)$ emerging at the phase transition temperature, which magnitude and sharpness noticeably decreases, and the position shifts to the higher temperatures with increasing E_0. Such behavior is typical for smearing of the first-order FEPT region by an external field.

The static dependences $\Delta T_{EC}(T)$ are shown in Fig. 5(d) for different E_0. For all E_0 and $T < 250$ K ΔT_{EC} is nonzero, but rather small. For $E_0 = 0.01$ V/nm, all negative values of ΔT_{EC} in vicinity of 280 K (the bottom part of curve 1) correspond to the unstable S-shaped region of polarization curve 1 in Fig. 5(a). This unstable static solution is rather an artifact, but may become observable in the situations, when unstable polarization can be observed (e.g., in the case of strong pinning in the range of temperature hysteresis). For $E_0 \geqslant 0.1$ V/nm, the rise of ECE starts at temperatures above 200 K, and its rate increases with electric field (see curves 2–4). At $T \approx 315$ K, ΔT_{EC} abruptly reaches the maximum of 2–3 K, which position slightly shifts towards higher temperatures with the increasing electric field. Then ΔT_{EC} gradually decreases (see curves 2–4). The temperature range of nonzero positive ΔT_{EC} significantly broadens with increasing E_0 (compare the shape of the maxima for the curves 2–4). The behavior of ECE correlates with the $P(T)$ behavior (curves 2–4 in Fig. 5a) and reflects FEPT smearing at high electric field. Note that the temperature hysteresis of negative $\Delta T_{EC}(T)$, existing for small E_0, disappears with increasing E_0 [see black solid and dotted curves in Fig. 5(d)].

Size dependences $P(R)$, $\varepsilon_{NP}(R)$, $\Pi(R)$, and $\Delta T_{EC}(R)$ calculated for several amplitudes of the external field, E_0 and $T = 293$ K are shown in Figs. 6(a)–6(d). These dependences correlate with the T dependences $P(T)$, $\varepsilon_{NP}(T)$, $\Pi(T)$, and $\Delta T_{EC}(T)$ shown in Figs. 4(a)–4(d), since $T_{cr} \sim 1/R$ per Eqs. (5b) and (8). The "size hysteresis", defined as the distance (in nanometers) between solid and dotted vertical lines, is the widest for the smallest E_0, and it narrows and disappears when E_0 increases above the critical value E_{cr}, that is about 0.1 V/nm at 293 K [compare solid and dashed curves 1–4 in Fig. 6(a)]. The origin of the effect is a thermodynamic bistability, and so it disappears with the frequency increase above the critical value, which is temperature- and field-dependent. The bistability region corresponds to the vicinity of the temperature-dependent critical radius R_{cr} given by Eq. (11). The static dependences for small E_0 contain the unstable S-shaped regions, which width strongly decreases with E_0 increase [compare solid and dashed curves 1 and 2 in Fig. 6(a)]. The dependences shown in Fig. 6(a) illustrate the scenario of the first-order size-induced FEPT. Correlating with Fig. 6(a), Figs. 6(b) and 6(c) show sharp maxima of $\varepsilon_{NP}(R)$ and $\Pi(R)$ emerging at the critical radius. With increasing E_0 the width of the $\varepsilon_{NP}(R)$ peak significantly decreases [curves 1–3 in Fig. 6(b)], while the width of the $\Pi(R)$ peak remains almost unchanged [curves 1–3 in Fig. 6(c)]. These peaks disappear for the strong enough field E_0 [curves 4 in Figs. 6(d) and 6(c)].

Size dependences $\Delta T_{EC}(R)$ calculated at $T = 293$ K, low frequency ($\omega = 2 \times 10^4$ s^{-1}), and several amplitudes E_0 are shown by solid curves in Fig. 6(d). They look very different for small ($E_0 < 0.1$ V/nm) and big ($E_0 \gg 0.1$ V/nm) amplitudes of E_{ext} [compare curves 1 and 2 with curves 3 and 4 in Fig. 6(d)]. The $\Delta T_{EC}(R)$ behavior strongly correlates with the $P(R)$ behavior shown in Fig. 6(a). In particular, the size hysteresis of $\Delta T_{EC}(R)$ disappears for E_0 larger than the critical value $E_{cr} \approx 0.1$V/nm.

At first let us analyze the dynamic dependences $\Delta T_{EC}(R)$ calculated at $\omega = 2 \times 10^4$ s^{-1}. For $E_0 \ll 0.1$ V/nm,, ΔT_{EC} abruptly increases at $R \approx R_{cr}$ from zero values to rather small positive values ~0.2 K in the region of polarization hysteresis and then exponentially decreases with R increasing [see solid curves 1 and 2 in Fig. 6(d)]. For $E_0 \geqslant 0.5$ V/nm, ΔT_{EC} gradually reaches 1–2 K at small $R < R_{cr}$, abruptly decreases above the critical radius and tends to zero with R increasing [see solid curves 3 and 4 in Fig. 6(d)]. Thus the region of nonzero $\Delta T_{EC}(R)$ is widest for the smallest E_0 and becomes significantly narrower with E_0 increase. The negative ECE calculated for the static case $\omega = 0$ (dashed curves 1 and 2) corresponds to the unstable solution and disappears at finite ω. As can be seen from the Fig. 6(d), we can control the shape, magnitude and width of $\Delta T_{EC}(R)$ peak by changing the electric field amplitude.

As follows from Eqs. (5b) and (5c), $T_{cr}(R, \Lambda) \to T_C^*$ and $\eta(R, \Lambda) \to 0$ in the limit $\varepsilon_{IF}(R/\Lambda) \to \infty$ corresponding to the bulk material with $R \to \infty$. Note that the field term in Eq. (5a) vanishes for $\eta(R, \Lambda) \to 0$, making the study of external field influence impossible in the limit $R \to \infty$ (infinite sphere has no electrodes). Strictly speaking, this circumstance does not allow a quantitative comparison of the magnitude of the EC response of the particles and the bulk sample, since the EC exists only at nonzero values of the external electric field. However other studied physical quantities, such as remnant polarization, linear dielectric permittivity, and PE coefficient, exist under the absence of external field. In order to understand from which radius the difference between the dependencies for the nanoparticle and the bulk material becomes negligible, the asymptotes in Fig. 6 for the smallest $E_0 = 0.01$ V/nm. As one can see, the dependences are similar to those for bulk materials at particle radius larger than 20 nm.

V. SIZE EFFECT OF PYROELECTRIC AND ELECTROCALORIC ENERGY CONVERSION

A. Size effect of pyroelectric figures of merit

For better displaying pyroelectric energy conversion it is convenient to consider the corresponding figures of merit (FoM) of pyroelectric materials. According to the operation modes of pyroelectric convertors [43,83–85], the current (F_I) and voltage (F_V) FoM have been introduced:

$$F_I = -\frac{\Pi}{c_P},\ F_V = -\frac{\Pi}{\varepsilon_0 \varepsilon c_P}. \tag{12a}$$

Here, $c_P = \rho C_P$ is the volume heat capacity and ρ is the density of the PE material.

In the energy conversion operation mode, a PE convertor of the capacity type generates a pyrocharge Q_π during a thermal cycle. At that, the electric energy generated during the heating/cooling cycle is proportional to ${Q_\pi}^2$. If the PE convertor is imposed to an incident radiation, the electric energy generated during the thermal cycle is proportional to the square of the pyrovoltage ${U_\pi}^2$. For both these cases, two different energy conversion FoM, $F_{\rm EQ}$ and $F_{\rm EU}$, have been proposed [85,86]:

$$F_{\rm EQ} = \frac{\Pi^2}{\varepsilon_0 \varepsilon}, \quad F_{\rm EU} = \frac{\Pi^2}{\varepsilon_0 \varepsilon c_P^2} \tag{12b}$$

The efficiency of the PE energy conversion is defined by the pyroelectric (electrothermal) coupling factor [85,86]:

$$k_{\rm PE}^2 = \frac{\Pi^2 T}{c_P \varepsilon_0 \varepsilon}, \tag{12c}$$

where T is the ambient temperature. The derivation details of expressions (9b) and (9c) are given in Appendix D in Ref. [58].

Expressions (9) for the PE FoM and coupling factor are valid for a freely suspended ferroelectric layer, and should be modified for nanocomposites, hybrid, or/and layered nanosystems. In accordance with the theory of finite size effects in ferroelectric nanomaterials [87], the form of basic expressions relatively often remains unchanged, but the parameters are substituted by effective ones. Hence, we introduce the PE FoMs and coupling constant for nanoparticles (NP) in the following form:

$$F_I = \frac{-\Pi}{c_{\rm NP}}, \quad F_f = \frac{-\Pi}{\varepsilon_0 \varepsilon_{\rm NP}}, \quad K_{\rm PE} = \frac{\Pi^2}{\varepsilon_0 \varepsilon_{\rm NP} c_{\rm NP}},$$
$$F_{\rm EQ} = \frac{\Pi^2}{\varepsilon_0 \varepsilon_{\rm NP}}, \quad F_{\rm EU} = \frac{\Pi^2}{\varepsilon_0 \varepsilon_{\rm NP} c_{\rm NP}^2}. \tag{13}$$

The nanoparticle volume heat capacity, $c_{\rm NP} = \rho C_P^{\rm NP}$, introduced in Eqs. (13), is a temperature- and size- dependent quantity. Figures 7 and 8 present temperature dependences of the values (13) calculated for different particle radii R and external electric field amplitude E_0.

Static temperature dependences of the specific heat variation $\delta C_P \equiv C_P - C_P^0$, PE FoMs F_I, F_f, $F_{\rm EQ}$, $F_{\rm EU}$, and coupling constant $K_{\rm PE}$ calculated for several R and relatively small $E_0 \ll E_{\rm cr}$ are shown in Figs. 7(a)–7(f). Dotted vertical lines with arrows show thermodynamically stable paths. The hysteresis region of the temperature dependences, defined as the distance between the two dashed lines, decreases and shifts towards higher temperatures with increasing the particle radius. It should be noted that the positions of the hysteresis for δC_P and all FoM are the same and completely coincide with the position of the $P(T)$ hysteresis in Fig. 4(a). $F_f(T)$ shows a maximum within the temperature hysteresis region, which magnitude does not depend on the particle size [Fig. 7(c)]. This is related to similar character of $\Pi(T)$ and $\varepsilon_{\rm NP}(T)$ divergences [Figs. 4(b) and 4(c)]. Temperature dependences of other parameters [Figs. 7(b)–7(f)] have either divergences or very sharp maxima at the edges of the temperature hysteresis region, which are slightly suppressed for F_I, $K_{\rm PE}$,and $F_{\rm EU}$ due to the increased δC_P in the region [Fig. 7(a)].

Static temperature dependences of δC_P, F_I, F_f, $K_{\rm PE}$, $F_{\rm EQ}$, and $F_{\rm EU}$ calculated for several amplitudes of the external field E_0 and $R = 10$ nm are shown in Figs. 8(a)–8(f). Dotted curves show thermodynamically unstable regions, where the temperature hysteresis exists. The temperature hysteresis disappears for electric fields above the critical value, $E_0 > E_{\rm cr}$, where $E_{\rm cr}$ is about 0.1 V/nm for $R = 10$ nm.

The temperature dependences of F_I, $K_{\rm PE}$, $F_{\rm EQ}$, and $F_{\rm EU}$ [Figs. 8(b) and 8(d)–8(f)] have either divergences or very sharp maxima at the edges of temperature hysteresis region. The temperature hysteresis for F_I, $K_{\rm PE}$, $F_{\rm EQ}$, and $F_{\rm EU}$ exists at weak fields $E_0 \ll E_{\rm cr}$ (see black curves). The hysteresis region disappears for $E_0 > E_{\rm cr}$ (see curves 2) and corresponding dependences are characterized by the maxima shifted towards higher temperatures under electric field increase (see curves 3 and 4). The increasing electric field also leads to the decrease of F_I,$F_{\rm EQ}$, $F_{\rm EU}$, and $K_{\rm PE}$ maximal values.

The temperature dependence of F_f does not have a divergence even at small $E_0 \ll E_{\rm cr}$, but has a maximum within the temperature hysteresis. Also F_f is characterized by the absence of hysteresis for $E_0 > E_{\rm cr}$, and the increase of the electric field leads to the shift of F_f maximum without affecting its value [see curves 2–4 in Fig. 8(c)].

We would like to underline the evident similarity between the temperature dependences of $F_{\rm EQ}$ and $F_{\rm EU}$ [Figs. 7(e), 7(f) and 8(e), 8(f)]. This similarity originates from the proportionality of both $F_{\rm EQ}$ and $F_{\rm EU}$ to $\frac{\Pi^2}{\varepsilon_0 \varepsilon_{\rm NP}}$ [see Eqs. (13)], as well as from the relatively weak temperature dependence of the heat capacity, $C_P = \delta C_P(T, R) + C_P^0$, since $\delta C_P(T, R) \ll C_P^0$ outside the immediate vicinity of the size-induced transition to the ferroelectric phase. At that external field strongly broadens and suppresses the maximum of $\delta C_P(T, R)$ with retention of sharp character of δC_P dependence in intermediate temperature range [compare curves 1–4 in Figs. 7(a) and 8(a)].

To resume the subsection, the results shown in Figs. 7 and 8 illustrate the possibility to control PE performances using the dependences of corresponding FoM and coupling factor on operating temperature, external electric field, and nanoparticle size.

B. Size effect of electrocaloric coefficient hysteresis

Let us study the size effect and frequency features of EC coefficient of ferroelectric nanoparticles, defined as the derivative of EC temperature change on external electric field [34,36],

$$\Sigma = \frac{d\Delta T_{\rm EC}}{dE_{\rm ext}}. \tag{14}$$

The size effect of $\Sigma(E_{\rm ext})$ can be important for ECE applications. Field dependence of Σ calculated for several radii of $BaTiO_3$ nanoparticle and two frequencies are shown in Figs. 9(a)–9(d).

In accordance with the field dependence $\Delta T_{\rm EC}(E_{\rm ext})$ shown in Fig. 3(d), the dependence $\Sigma(E_{\rm ext})$ is symmetrical with respect to the coordinate origin [Figs. 9(a) and 9(c)]. The field dependences $\Sigma(E_{\rm ext})$ are characterized by the presence of a maximum, which position shifts to higher fields with increasing the nanoparticle size [see curves 1–4 in Figs. 9(b) and 9(d)]. As we have discussed already, this maximum corresponds to the thermodynamic coercive field, which means that

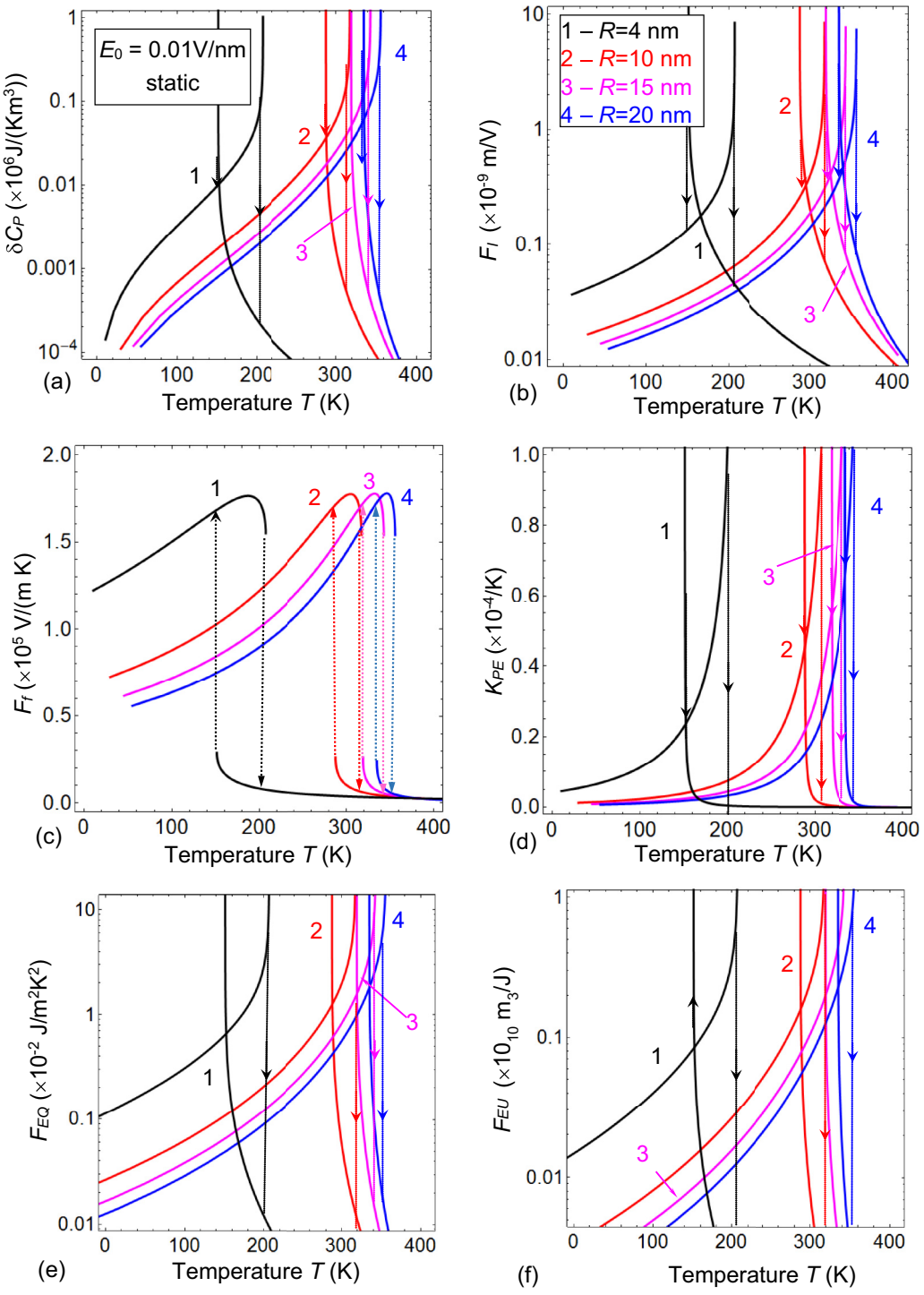

FIG. 7. Static temperature dependences of specific heat variation $\delta C_P \equiv C_P - C_P^0$ (a), and PE performances F_I (b), F_f (c), $K_{\rm PE}$ (d), $F_{\rm EQ}$ (e), and $F_{\rm EU}$ (f) calculated for several radii of $BaTiO_3$ nanoparticles $R = 4$, 10, 15, and 20 nm (curves 1–4). External field amplitude $E_0 = 0.01$ V/nm. Dotted vertical lines with arrows show thermodynamically stable paths under the temperature increase or decrease. Other parameters are the same as in Fig. 3.

the field induced entropy change is maximal at the polarization reversal in the single domain state. When the polarization switching occurs just via polarization rotation, the increasing entropy can be related to the appearance of the polarization component perpendicular to the electric field direction. Similar effect has been observed in antiferroelectrics [88]. The appearance of a polydomain state in vicinity of the coercive field is quite probable in experiment, but it is not the case for a chosen small Λ and high $\varepsilon_{\rm IF}$.

Comparing the field dependences of $\Sigma(E_{\rm ext})$ shown in Figs. 9(c) and 9(d), it is seen that the widths of maxima increase and their amplitudes decrease with increasing frequency. The splitting of $\Sigma(E_{\rm ext})$ maximum is more pronounced for particles with a size of 10 nm, close to the critical

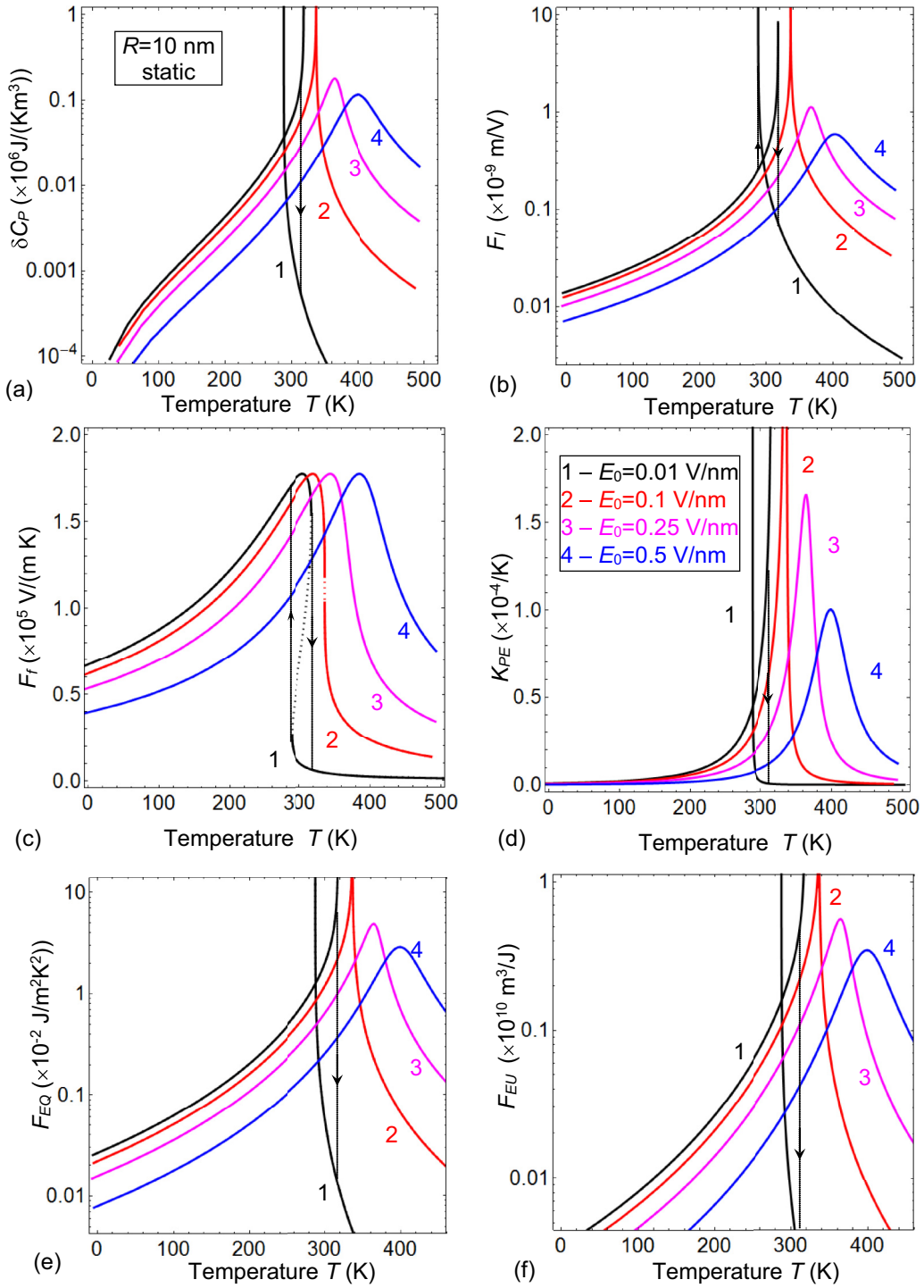

FIG. 8. Static temperature dependences of specific heat variation $\delta C_P \equiv C_P - C_P^0$ (a), and PE performances F_I (b), F_f (c), $K_{\rm PE}$ (d), $F_{\rm EQ}$(e), and $F_{\rm EU}$ (f) calculated for of $BaTiO_3$ nanoparticles with radius $R = 10$ nm and different values of external field $E_0 = 0.01$, 0.1, 0.25, and 0.5 V/nm (curves 1–4). Other parameters are the same as in Fig. 3.

one ≈8 nm. The smallest paraelectric particle shows a maximum on the $\Sigma(E_{\rm ext})$ dependence, which might be attributed to the critical point in a field-temperature phase diagram [89]. The smallest 4-nm particles, which size is well below the critical size (∼ 8 nm at room temperature), are characterized by a zero value of Σ at the zero field (curve 1), unlike the situation for nanoparticles of a larger diameter (curves 2–4), that corresponds to $\Delta T_{\rm EC}(E_{\rm ext})$ shown in Fig. 3(d).

Analysis of the radius and electric field dependences of $\Sigma(E_{\rm ext})$ presented in this subsection shows the possibility to control the effectiveness of EC energy conversion by changing the radius of a nanoparticle.

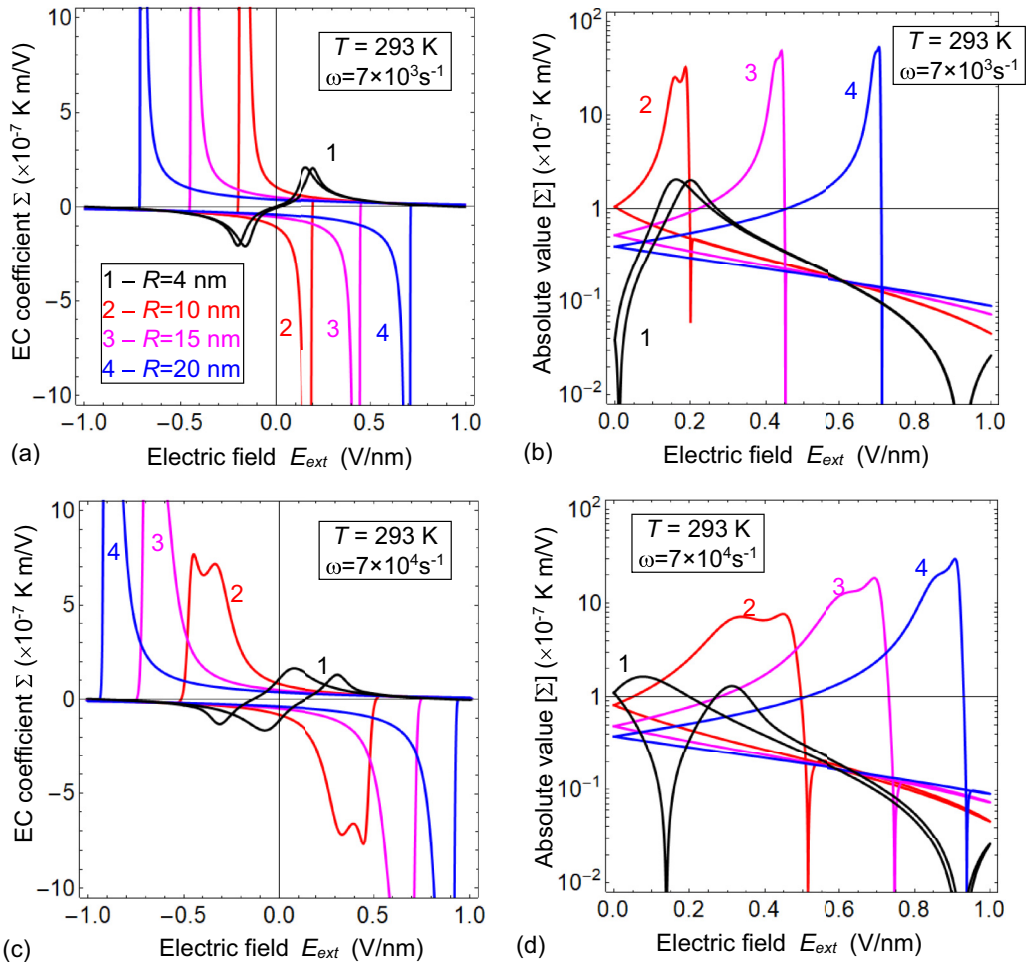

FIG. 9. Dependences of EC coefficient Σ [(a) and (c)] and its absolute value |Σ| in logarithmic scale [(b) and (d)] on external electric field calculated for several radii $R = 4$, 10, 15, and 20 nm of $BaTiO_3$ nanoparticle (curves 1–4), $T = 293$ K, frequency $\omega = 7 \times 10^3$ [(a) and (b)] and 7×10^4 s^{-1} [(c) and (d)]. Other parameters are the same as in Fig. 3.

VI. DISCUSSION AND CONCLUSION

Using LGD theory, we calculated and analyzed the dependences of polarization, dielectric permittivity, pyroelectric, and electrocaloric properties on external electric field, temperature, and radius of a spherical single-domain ferroelectric nanoparticle covered by a semiconducting shell and placed in a dielectric medium. The chosen geometry is typical for the theoretical consideration of ferroelectric nanocomposites in the effective medium approximation, if the volume fraction of the nanoparticles is relatively small (e.g., less than 10%).

For numerical simulations we considered $BaTiO_3$ nanoparticles placed in a polymer matrix, since such nanocomposites already exist and regarded attractive for pyroelectric and electrocaloric applications. We have chosen $BaTiO_3$ because it undergoes the first-order phase transition from the ferroelectric to paraelectric phase, and this fact adds additional interesting peculiarities of PE and EC properties, such as the temperature and size-induced hysteresis, in comparison with the ferroelectric materials undergoing the second-order phase transition. It should be noted that analytical expressions derived in the paper can be applied for any other ferroelectric material.

We established how the particle size determines the behavior PEE and ECE in the single-domain ferroelectric nanoparticles with the first order phase transition. We show that one can induce the maxima of PE coefficient and EC temperature variation, control their width and height by changing the particle size, as well as tune the voltage and temperature intervals for which PEE or/and ECE are maximal. Also, we revealed that it is possible to select the interval of particle radii, for which PE and/or EC energy conversion are maximal at room temperature. Corresponding trends based on our calculations are summarized in Table II.

Allowing for the generality of performed consideration for ferroelectric nanoparticles with the first order phase transition of displacement type the obtained results are valid not only for $BaTiO_3$, but for many other ferroelectrics with the same type of phase transition [e.g., $PbTiO_3$, (Pb, Zr)TiO_3:La, $KNbO_3$, $BiFeO_3$]. It follows from Table II that PE coefficient, FoM, and energy conversion can be anomalously large for the particles with size near the critical one. The electrocaloric temperature change ΔT_{EC} and its derivative on external electric field have maximal value around the critical size, but they are not large, because the field mainly smears temperature dependence of polarization.

TABLE II. Size effect of polar, dielectric, PE and EC properties of single-domain ferroelectric nanoparticles with the first-order FEPT.

Nanoparticle property	Size effect at small static external electric fields ($0 \leqslant E \ll E_{cr}$, $\omega = 0$)	Influence of external quasistatic electric fields E ($0 \ll E < 10\,E_{cr}$, ω is zero or small[c])
Ferroelectric polarization $P(T,R)$ [Figs. 3(a), 4(a), 5(a), and 6(a)]	$P(T,R)$ disappears (at $E = 0$) or becomes rather small (at $E > 0$) for temperatures $T > T_{cr}(R)$[a] and sizes $R < R_{cr}(T)$. [b] Temperature and size hysteresis of $P(T,R)$ exists near $T \approx T_{cr}(R)$ and $R \approx R_{cr}(T)$, respectively.	External fields comparable with E_{cr} induce irreversible polarization at $T > T_{cr}(R)$, the value of which increases with E increasing. Increasing the field in the range $0 \ll E < 5\,E_{cr}$ smooth out all temperature and size features of $P(T,R)$. The temperature hysteresis disappears at $E \geqslant E_{cr}$. $P(E)$ loops become wider and metastable states disappear with ω increase.
Dielectric permittivity $\varepsilon_{NP}(T, R)$ [Figs. 3(b), 4(b), 5(b), and 6(b)]	$\varepsilon_{NP}(T, R)$ is maximal (at $E > 0$) or diverges (at $E = 0$) at $T = T_{cr}(R)$ and $R = R_{cr}(T)$, respectively. Temperature and size hysteresis of $\varepsilon_{NP}(T, R)$ exists near $T \approx T_{cr}(R)$ and $R \approx R_{cr}(T)$, respectively.	Increasing the field in the range $0 \ll E < 5\,E_{cr}$ significantly broadens $\varepsilon_{NP}(T)$ maximum, decreases the maximum height and shifts its R-dependent position to higher T. The temperature hysteresis disappears at $E \geqslant E_{cr}$. The maximum (attributed to the FEPT) disappears at $E \gg E_{cr}$.
PE coefficient, $\Pi(T, R)$ [Figs. 3(c), 4(c), 5(c), and 6(c)]	$\Pi(T, R)$ is maximal (at $E > 0$) or diverges (at $E = 0$) at $T = T_{cr}(R)$ and $R = R_{cr}(T)$. $\Pi(T, R)$ almost vanishes at $T > T_{cr}(R)$ and $R < R_{cr}(T)$. Temperature and size hysteresis of $\Pi(T, R)$ exists near $T \approx T_{cr}(R)$ and $R \approx R_{cr}(T)$, respectively.	Increasing the field in the range $0 \ll E < 5\,E_{cr}$ significantly broadens $\Pi(T)$ maximum, decreases the maximum height and shifts its R-dependent position to higher T. The temperature hysteresis disappears at $E \geqslant E_{cr}$.
PE detection FoM, $F_I(T, R)$ and $F_f(T, R)$ [Figs. 7(b), 7(c), 8(b), and 8(c)]	FoM are maximal at $T = T_{cr}(R)$. The temperature hysteresis exists close to $R = R_{cr}(T)$. The hysteresis width increases with R decrease.	Increasing the field in the range $0 \ll E < 5\,E_{cr}$ significantly broadens $F_I(T)$ and $F_f(T)$ maxima and shifts their R-dependent position to higher T. The field increasing decreases the height of $F_I(T)$ maximum, but does not change the height of $F_f(T)$ maximum. The temperature hysteresis of $F_I(T)$ and $F_f(T)$ disappears at $E \geqslant E_{cr}$.
PE energy conversion FoM $F_{EQ}(T, R)$ and $F_{EU}(T, R)$, and coupling factor $K_{PE}(T, R)$ [Figs. 7(d)–7(f) and 8(d)–8(f)]	The factors are maximal at $T = T_{cr}(R)$. The temperature hysteresis exists close to $R = R_{cr}(T)$. The hysteresis width increases with R decrease.	Increasing the field in the range $0 \ll E < 5\,E_{cr}$ significantly broadens $F_{EQ}(T)$, $F_{EU}(T)$, and $K_{PE}(T)$ maxima, decreases their height and shifts the maxima position to higher T. The temperature hysteresis of PE energy conversion factors disappears at $E \geqslant E_{cr}$.
EC temperature change, $\Delta T_{EC}(T,R,E)$ [Figs. 3(d), 4(d)–4(f), 5(d), and 6(d)]	$\Delta T_{EC}(T, R)$ is zero at $E = 0$. At $0 < E \ll E_{cr}$ $\Delta T_{EC}(T)$ is maximal at $T = T_{cr}(R)$. $\Delta T_{EC}(R)$ is positive below $R_{cr}(T)$ and changes its sign depending on the field magnitude at $R > R_{cr}(T)$. Temperature and size hysteresis of $\Delta T_{EC}(T,R,E)$ exists near $T \approx T_{cr}(R)$ and $R \approx R_{cr}(T)$, respectively.	Increasing the field in the range $0 \ll E < 5\,E_{cr}$ significantly broadens ΔT_{EC} maximum, increases its height and shifts its R-dependent position to higher $T > T_{cr}(R)$. The temperature hysteresis disappears at $E \geqslant E_{cr}$. The frequency increase narrows the region of nonzero ΔT_{EC}.
EC coefficient $\Sigma(T,R,E)$ (Fig. 9)	$\Sigma(R)$ is close to zero at $R < R_{cr}(T)$, maximal at $R = R_{cr}(T)$ and decreases with R increase at $R > R_{cr}(T)$. Narrowing of $\Sigma(E)$ hysteresis width and suppression of its maxima at $E = E_{coercive}$ occurs with R decrease.	Increasing the field in the range $0 \ll E < 5\,E_{cr}$ induces nonzero $\Sigma(E)$ at $R < R_{cr}(T)$. $\Sigma(E)$ hysteresis disappears at $E \gg E_{cr}$. The coercive field of $\Sigma(E)$ hysteresis strongly increases with R increase and then saturates to the bulk value. The frequency increase significantly broadens $\Sigma(E)$ maxima at coercive field, decreases peak values and shift them to higher fields.

[a] $T_{cr}(R)$ is the critical temperature of the FEPT for a nanoparticle of radius R, which decreases with R decrease, increases with E increase, and can be estimated from Eq. (5b) for small fields $0 \leqslant E \ll E_{cr}$. The FEPT at $T = T_{cr}(R)$ smears and eventually disappears at $E \gg E_{cr}$.

[b] $R_{cr}(T)$ is the particle critical size at a temperature T, which decreases with T and E increase, and can be estimated from Eq. (11) for small fields $0 \leqslant E \ll E_{cr}$.$R_{cr}(T)$ disappears at $E \gg E_{cr}$.

[c] The frequency effect is mentioned in the table only for those few cases, which are studied in the paper. The systematic study of ω effect will be performed elsewhere.

To summarize, the obtained analytical results demonstrate possibilities to control the pyroelectric and electrocaloric properties of ferroelectric nanocomposites, and the working performances (figures of merits, energy conversion efficiency) of PE and EC convertors by changing the nanoparticle sizes, and tuning the amplitude and frequency of the external electric field. This is important for advanced cryogenic and energy harvesting applications. Using the ferroelectrics undergoing the first-order phase transition adds additional interesting peculiarities of the PE and EC properties, such as the temperature and size-induced hysteresis, in comparison with ferroelectric materials undergoing the second-order phase transition.

ACKNOWLEDGMENTS

A.N.M. expresses her deepest gratitude to S. M. Ryabchenko (NASU), V. Yu. Reshetnyak (KNU), and R. Hertel (CNRS) for stimulating discussions about the nature of effective screening length, electrostatic problems, and polarization vortexes. Authors are especially grateful to the Referees for useful remarks and stimulating discussions. A.N.M. work was partially supported by the National Academy of Sciences of Ukraine (Projects No. 0118U003375 and No. 0117U002612) and by the Program of Fundamental Research of the Department of Physics and Astronomy of the National Academy of Sciences of Ukraine (Project No. 0117U000240). M.V.S. acknowledges RFBR grant 17-08-01374_a and Russian academic excellence project "5–100" for Sechenov First Moscow State Medical University. A portion of FEM was conducted at the Center for Nanophase Materials Sciences, which is a DOE Office of Science User Facility (CNMS Proposal ID: 257). This project has received funding from the European Union's Horizon 2020 research and innovation programme under the Marie Skłodowska-Curie Grant Agreement No. 778070.

A.N.M. and V.V.S. generated research idea and proposed a model. A.N.M. stated the problem, derived analytical expressions jointly with E.A.E., interpreted results and wrote the manuscript draft. E.A.E. jointly with H.V.S. wrote the codes and performed numerical calculations. M.D.G., N.V.M., V.V.S., and other co-authors densely worked on the results discussion and manuscript improvement.

[1] Y. L. Tang, Y. L. Zhu, X. L. Ma, A. Y. Borisevich, A. N. Morozovska, E. A. Eliseev, W. Y. Wang, Y. J. Wang, Y. B. Xu, Z. D. Zhang, and S. J. Pennycook, Observation of a periodic array of flux-closure quadrants in strained ferroelectric $PbTiO_3$ films, Science **348**, 547 (2015).

[2] A. N. Morozovska, E. A. Eliseev, and S. V. Kalinin, Topological defects in ferroic materials, in *Topological Structures in Ferroic Materials*, edited by J. Seidel, Springer Series in Materials Science Vol. 228 (Springer International Publishing, Switzerland, 2016), pp. 181–197.

[3] S. Zhang, Y. Zhu, Y. Tang, Y. Liu, S. Li, M. Han, Jinyuan Ma, B. Wu, Z. Chen, S. Saremi, and X. Ma, Giant polarization sustainability in ultrathin ferroelectric films stabilized by charge transfer, Adv. Mater. **29**, 1703543 (2017).

[4] S. He, G. Liu, Y. Zhu, X. Ma, J. Sun, S. Kang, S. Yan, Y. Chen, L. Mei, and J. Jiao, Impact of interfacial effects on ferroelectric resistance switching of $Au/BiFeO_3/Nb : SrTiO_3(100)$ Schottky junctions, RSC Adv. **7**, 22715 (2017).

[5] S. Zhang, X. Guo, Y. Tang, D. Ma, Y. Zhu, Y. Wang, S. Li, M. Han, D. Chen, J. Ma, B. Wu, and X. Ma, Polarization rotation in ultrathin ferroelectrics tailored by interfacial oxygen octahedral coupling, ACS Nano **12**, 3681 (2018).

[6] S. V. Kalinin, Y. Kim, D. Fong, and A. N. Morozovska, Surface-screening mechanisms in ferroelectric thin films and their effect on polarization dynamics and domain structures, Rep. Prog. Phys. **81**, 036502 (2018).

[7] D. Yadlovker and S. Berger. Uniform orientation and size of ferroelectric domains, Phys. Rev. B **71**, 184112 (2005).

[8] D. Yadlovker and S. Berger, Reversible electric field induced nonferroelectric to ferroelectric phase transition in single crystal nanorods of potassium nitrate, Appl. Phys. Lett. **91**, 173104 (2007).

[9] M. H. Frey and D. A. Payne, Grain-size effect on structure and phase transformations for barium titanate, Phys. Rev. B **54**, 3158 (1996).

[10] Z. Zhao, V. Buscaglia, M. Viviani, M. T. Buscaglia, L. Mitoseriu, A. Testino, M. Nygren, M. Johnsson, and P. Nanni, Grain-size effects on the ferroelectric behavior of dense nanocrystalline $BaTiO_3$ ceramics, Phys. Rev. B **70**, 024107 (2004).

[11] A. V. Drobnich, A. A. Molnar, A. V. Gomonnai, Yu. M. Vysochanskii, and I. P. Prits, The effect of size factor on the phase transition in $Sn_2P_2S_6$ crystals: Experimental data and simulation in ANNNI model, Condens. Matter. Phys. **6**, 205 (2003).

[12] E. Erdem, H.-Ch. Semmelhack, R. Bottcher, H. Rumpf, J. Banys, A. Matthes, H.-J. Glasel, D. Hirsch, and E. Hartmann, Study of the tetragonal-to-cubic phase transition in $PbTiO_3$ nanopowders, J. Phys.: Condens. Matter. **18**, 3861 (2006).

[13] T. Yu, Z. X. Shen, W. S. Toh, J. M. Xue, and J. Wang, Size effect on the ferroelectric phase transition in $SrBi_2Ta_2O_9$ nanoparticles, J. Appl. Phys. **94**, 618 (2003).

[14] I. S. Golovina, V. P. Bryksa, V. V. Strelchuk, I. N. Geifman, and A. A. Andriiko, Size effects in the temperatures of phase transitions in $KNbO_3$ nanopowder, J. Appl. Phys. **113**, 144103 (2013).

[15] U. Idehenre, Y. A. Barnakov, S. A. Basun, and D. R. Evans, Spectroscopic studies of the effects of mechanochemical synthesis on $BaTiO_3$ nanocolloids prepared using high-energy ball-milling, J. Appl. Phys. **124**, 165501 (2018).

[16] Y. A. Barnakov, I. U. Idehenre, S. A. Basun, T. A. Tyson, and D. R. Evans, Uncovering the mystery of ferroelectricity in zero dimensional nanoparticles, Nanoscale Adv. **1**, 664 (2019).

[17] P. Perriat, J. C. Niepce, and G. Caboche, Thermodynamic considerations of the grain size dependency of material properties: A new approach to explain the variation of the dielectric permittivity of $BaTiO_3$ with grain size, J. Therm. Anal. Calorim. **41**, 635 (1994).

[18] H. Huang, C. Q. Sun, Z. Tianshu, and P. Hing, Grain-size effect on ferroelectric $Pb(Zr_{1-x}Ti_x)O_3$ solid solutions

induced by surface bond contraction, Phys. Rev. B **63**, 184112 (2001).

[19] M. D. Glinchuk, E. A. Eliseev, and A. N. Morozovska, Superparaelectric phase in the ensemble of noninteracting ferroelectric nanoparticles, Phys. Rev. B **78**, 134107 (2008).

[20] W. Ma, Surface tension and Curie temperature in ferroelectric nanowires and nanodots, Appl. Phys. A **96**, 915 (2009).

[21] V. V. Khist, E. A. Eliseev, M. D. Glinchuk, D. V. Karpinsky, M. V. Silibin, and A. N. Morozovska, Size effects of ferroelectric and magnetoelectric properties of semi-ellipsoidal bismuth ferrite nanoparticles, J. Alloy. Compd. **714**, 303 (2017).

[22] J. J. Wang, X. Q. Ma, Q. Li, J. Britson, and L.-Q. Chen, Phase transitions and domain structures of ferroelectric nanoparticles: Phase field model incorporating strong elastic and dielectric inhomogeneity, Acta Mater. **61**, 7591 (2013).

[23] J. J. Wang, E. A. Eliseev, X. Q. Ma, P. P. Wu, A. N. Morozovska, and L.-Q. Chen, Strain effect on phase transitions of $BaTiO_3$ nanowires, Acta Mater. **59**, 7189 (2011).

[24] E. A. Eliseev, A. N. Morozovska, M. D. Glinchuk, and R. Blinc, Spontaneous flexoelectric/flexomagnetic effect in nanoferroics, Phys. Rev. B **79**, 165433 (2009).

[25] E. A. Eliseev, V. V. Khist, M. V. Silibin, Y. M. Fomichov, G. S. Svechnikov, D. V. Karpinsky, V. V. Shvartsman, and A. N. Morozovska, Fixed volume effect on polar properties and phase diagrams of ferroelectric semi-ellipsoidal nanoparticles, Eur. Phys. J. B **91**, 150 (2018).

[26] A. N. Morozovska, M. D. Glinchuk, and E. A. Eliseev, Phase transitions induced by confinement of ferroic nanoparticles, Phys. Rev. B **76**, 014102 (2007).

[27] A. N. Morozovska, I. S. Golovina, S. V. Lemishko, A. A. Andriiko, S. A. Khainakov, and E. A. Eliseev, Effect of Vegard strains on the extrinsic size effects in ferroelectric nanoparticles, Phys. Rev. B **90**, 214103 (2014).

[28] A. N. Morozovska, Y. M. Fomichov, P. Maksymovych, Y. M. Vysochanskii, and E. A. Eliseev, Analytical description of domain morphology and phase diagrams of ferroelectric nanoparticles, Acta Mater. **160**, 109 (2018).

[29] Y. Liu, J. F. Scott, and B. Dkhil, Direct and indirect measurements on electrocaloric effect: Recent developments and perspectives, Appl. Phys. Rev. **3**, 031102 (2016).

[30] Y.-B. Ma, N. Novak, J. Koruza, T. Yang, Tongqing, K. Albe, and B.-X. Xu, Enhanced electrocaloric cooling in ferroelectric single crystals by electric field reversal, Phys. Rev. B **94**, 100104 (2016).

[31] X. Chen, W. Xu, B. Lu, T. Zhang, Q. Wang, and Q. M. Zhang, Towards electrocaloric heat pump—A relaxor ferroelectric polymer exhibiting large electrocaloric response at low electric field, Appl. Phys. Lett. **113**, 113902 (2018).

[32] A. V. Kimmel, O. T. Gindele, D. M. Duffy, and R. E. Cohen, Giant electrocaloric effect at the antiferroelectric-to-ferroelectric phase boundary in $PbZrTiO_3$, Appl. Phys. Lett. **115**, 023902 (2019).

[33] L. W. Martin and A. M. Rappe, Thin-film ferroelectric materials and their applications, Nat. Rev. Mater. **2**, 16087 (2016).

[34] S. Pandya, J. D. Wilbur, B. Bhatia, A. R. Damodaran, C. Monachon, A. Dasgupta, W. P. King, C. Dames, and L. W. Martin, Direct Measurement of Pyroelectric and Electrocaloric Effects in Thin Films, Phys. Rev. Appl. **7**, 034025 (2017).

[35] S. W. Smith, D. M. Henry, M. T. Brumbach, M. A. Rodriguez, and J. F. Ihlefeld, Thickness scaling of pyroelectric response in thin ferroelectric $Hf_{1-x}Zr_xO_2$ films, Appl. Phys. Lett. **113**, 182904 (2018).

[36] S. Pandya, G. A. Velarde, R. Gao, A. S. Everhardt, J. D. Wilbur, R. Xu, J. T. Maher, J. C. Agar, C. Dames, and L. W. Martin, Understanding the role of ferroelastic domains on the pyroelectric and electrocaloric effects in ferroelectric thin films, Adv. Mater. **31**, 1803312 (2018).

[37] M. T. Kesim, J. Zhang, S. P. Alpay, and L. W. Martin, Enhanced electrocaloric and pyroelectric response from ferroelectric multilayers, Appl. Phys. Lett. **105**, 052901 (2014).

[38] S. Kar-Narayan and N. D. Mathur, Direct and indirect electrocaloric measurements using multilayer capacitors, J. Phys. D **43**, 32002 (2010).

[39] S. Kar-Narayan, S. Crossley, X. Moya, V. Kovacova, J. Abergel, A. Bontempi, N. Baier, E. Defay, and N. D. Mathur, Direct electrocaloric measurements of a multilayer capacitor using scanning thermal microscopy and infra-red imaging, Appl. Phys. Lett. **102**, 032903 (2013).

[40] Y. Shi, L. Huang, A. K. Soh, G. J. Weng, S. Liu, and S. A. T. Redfern, A scaling law for distinct electrocaloric cooling performance in low-dimensional organic, relaxor and antiferroelectrics, Sci. Rep. **7**, 11111 (2017).

[41] S. Patel, A. Chauhan, J. Cuozzo, S. Lisenkov, I. Ponomareva, and R. Vaish, Pyro-paraelectric and flexocaloric effects in barium strontium titanate: A first principles approach, Appl. Phys. Lett. **108**, 162901 (2016).

[42] J. F. Nye, *Physical Properties of Crystals: Their Representation by Tensors and Matrices* (Clarendon Press, Oxford, 1957).

[43] S. B. Lang, *Sourcebook of Pyroelectricity* (Gordon & Breach Science, London, 1974).

[44] W. H. Clingman and R. G. Moore, Application of ferroelectricity to energy conversion processes, J. Appl. Phys. **32**, 675 (1961).

[45] E. Fatuzzo, H. Kiess, and R. Nitsche, Theoretical efficiency of pyroelectric power converters, J. Appl. Phys. **37**, 510 (1966).

[46] P. D. Thacher, Electrocaloric effects in some ferroelectric and antiferroelectric Pb(Zr, Ti)O_3 compounds, J. Appl. Phys. **39**, 1996 (1968).

[47] A. S. Mischenko, Q. Zhang, J. F. Scott, R. W. Whatmore, and N. D. Mathur, Giant electrocaloric effect in thin-film $PbZr_{0.95}Ti_{0.05}O_3$, Science **311**, 1270 (2006).

[48] R. Kumar and S. Singh, Giant electrocaloric and energy storage performance of $[(K_{0.5}Na_{0.5})NbO_3]_{(1-x)}$-$[LiSbO_3]_x$ nanocrystalline ceramics, Sci. Rep. **8**, 3186 (2018).

[49] D. Saranya, A. R. Chaudhuri, J. Parui, and S. B. Krupanidhi, Electrocaloric effect of PMN-PT thin films near morphotropic phase boundary, Bull. Mater. Sci. **32**, 259 (2009).

[50] J. F. Scott, Electrocaloric materials, Ann. Rev. Mater. Res. **41**, 229 (2011).

[51] M. C. Rose and R. E. Cohen, Giant Electrocaloric Effect Around T_C, Phys. Rev. Lett. **109**, 187604 (2012).

[52] X. Moya, S. Kar-Narayan, and N. D. Mathur, Caloric materials near ferroic phase transitions, Nat. Mat. **13**, 439 (2014).

[53] A. N. Morozovska, E. A. Eliseev, G. S. Svechnikov, and S. V. Kalinin, Pyroelectric response of ferroelectric nanowires: Size effect and electric energy harvesting, J. Appl. Phys. **108**, 042009 (2010).

[54] Y. K. Zeng, B. Li, J. B. Wang, X. L. Zhong, W. Wang, F. Wang, and Y. C. Zhou, Influence of vortex domain switching on

the electrocaloric property of a ferroelectric nanoparticle, RSC Adv. **4**, 30211 (2014).
[55] M. Liu and J. Wang, Giant electrocaloric effect in ferroelectric nanotubes near room temperature, Sci. Rep. **5**, 7728 (2015).
[56] C. Ye, J. B. Wang, B. Li, and X. L. Zhong, Giant electrocaloric effect in a wide temperature range in $PbTiO_3$ nanoparticle with double-vortex domain structure, Sci. Rep. **8**, 293 (2018).
[57] C. Xiqu and C. Fang, Study of electrocaloric effect in barium titanate nanoparticle with core–shell model, Physica B: Cond. Matt. **415**, 14 (2013).
[58] See Supplemental Material at http://link.aps.org/supplemental/10.1103/PhysRevMaterials.3.104414 for calculation details of the transition temperature, PEE, and ECE, and auxiliary figures are presented in Appendixes A, B, C, and D, respectively.
[59] A. K. Tagantsev and G. Gerra, Interface-induced phenomena in polarization response of ferroelectric thin films, J. Appl. Phys. **100**, 051607 (2006).
[60] I. P. Batra, P. Wurfel, and B. D. Silverman, New Type of First-Order Phase Transition in Ferroelectric Thin Films, Phys. Rev. Lett. **30**, 384 (1973).
[61] P. Wurfel and I. P. Batra, Depolarization effects in thin ferroelectric films, Ferroelectrics **12**, 55 (1976).
[62] M. Stengel and N. A. Spaldin, Origin of the dielectric dead layer in nanoscale capacitors, Nature (London) **443**, 679 (2006).
[63] M. Stengel, D. Vanderbilt, and N. A. Spaldin, First-principles modeling of ferroelectric capacitors via constrained displacement field calculations, Phys. Rev. B **80**, 224110 (2009).
[64] J. Wang, A. K. Tagantsev, and N. Setter, Size effect in ferroelectrics: Competition between geometrical and crystalline symmetries, Phys. Rev. B **83**, 014104 (2011).
[65] A. K. Tagantsev, G. Gerra, and N. Setter, Short-range and long-range contributions to the size effect in metal-ferroelectric-metal heterostructures, Phys. Rev. B **77**, 174111 (2008).
[66] J. Junquera and P. Ghosez, Critical thickness for ferroelectricity in perovskite ultrathin films, Nature (London) **422**, 506 (2003).
[67] G. B. Stephenson and M. J. Highland, Equilibrium and stability of polarization in ultrathin ferroelectric films with ionic surface compensation, Phys. Rev. B **84**, 064107 (2011).
[68] M. J. Highland, T. T. Fister, D. D. Fong, P. H. Fuoss, C. Thompson, J. A. Eastman, S. K. Streiffer, and G. B. Stephenson, Equilibrium Polarization of Ultrathin $PbTiO_3$ with Surface Compensation Controlled by Oxygen Partial Pressure, Phys. Rev. Lett. **107**, 187602 (2011).
[69] A. N. Morozovska, E. A. Eliseev, Y. A. Genenko, I. S. Vorotiahin, M. V. Silibin, Ye Cao, Y. Kim, M. D. Glinchuk, and S. V. Kalinin, Flexocoupling impact on the size effects of piezo- response and conductance in mixed-type ferroelectrics-semiconductors under applied pressure, Phys. Rev. B **94**, 174101 (2016).
[70] I. S. Vorotiahin, E. A. Eliseev, Q. Li, S. V. Kalinin, Y. A. Genenko, and A. N. Morozovska, Tuning the polar states of ferroelectric films via surface charges and flexoelectricity, Acta Mater. **137**, 85 (2017).
[71] E. A. Eliseev, I. S. Vorotiahin, Y. M. Fomichov, M. D. Glinchuk, S. V. Kalinin, Y. A. Genenko, and A. N. Morozovska, Defect driven flexo-chemical coupling in thin ferroelectric films, Phys. Rev. B **97**, 024102 (2018).
[72] A. N. Morozovska, V. V. Khist, M. D. Glinchuk, V. Gopalan, and E. A. Eliseev, Linear antiferrodistortive-antiferromagnetic effect in multiferroics: Physical manifestations, Phys. Rev. B **92**, 054421 (2015).
[73] F. Jona and G. Shirane, *Ferroelectric Crystals, International Series of Monographs on Solid State Physics* (Pergamon Press, Oxford, 1962).
[74] J. Kulek, I. Szafraniak, B. Hilczer, and M. Połomska, Dielectric and pyroelectric response of PVDF loaded with $BaTiO_3$ obtained by mechanosynthesis, J. Non Crys. Sol. **353**, 4448 (2007).
[75] X. Zhang, Y. Shen, Q. Zhang, L. Gu, Y. Hu, J. Du, Y. Lin, and C.-W. Nan, Ultrahigh energy density of polymer nanocomposites containing $BaTiO_3$@TiO_2 nanofibers by atomic-scale interface engineering, Adv. Mater. **27**, 819 (2015).
[76] J. Qian, R. Peng, Z. Shen, J. Jiang, F. Xue, T. Yang, L. Chen, and Y. Shen, Interfacial coupling boosts giant electrocaloric effects in relaxor polymer nanocomposites: In situ characterization and phase-field simulation, Adv. Mater. **31**, 1801949 (2019).
[77] J. Hlinka and P. Márton, Phenomenological model of a 90° domain wall in $BaTiO_3$-type ferroelectrics, Phys. Rev. B **74**, 104104 (2006).
[78] P. Marton, I. Rychetsky, and J. Hlinka, Domain walls of ferroelectric $BaTiO_3$ within the Ginzburg-Landau-Devonshire phenomenological model, Phys. Rev. B **81**, 144125 (2010).
[79] W. Ma and L. E. Cross, Flexoelectricity of barium titanate, Appl. Phys. Lett. **88**, 232902 (2006).
[80] I. Ponomareva, A. K. Tagantsev, and L. Bellaiche, Finite-temperature flexoelectricity in ferroelectric thin films from first principles, Phys. Rev. B **85**, 104101 (2012).
[81] Z. Y. Chen, Y. X. Su, Z. D. Zhou, L. S. Lei, and C. P. Yang, The influence of the electrical boundary condition on domain structures and electrocaloric effect of $PbTiO_3$ nanostructures, AIP Advances **6**, 055207 (2016).
[82] G. G. Wisemann, Electrocaloric effect in potassium dihydrogen phosphate, IEEE Trans. Electron. Dev. ED **16**, 588 (1969).
[83] S. B. Lang and D. K. Das-Gupta, Pyroelectricity: Fundamentals and applications, in *Handbook of Advanced Electronic and Photonic Materials and Devices* (Academic Press, San Diego, 2001), pp. 1–55.
[84] A. K. Batra and M. D. Aggarwal, *Pyroelectric Materials: Infrared Detectors, Particle Accelerators, and Energy Harvesters* (SPIE Press, Bellingham, Washington, USA, 2013).
[85] A. Thakre, A. Kumar, H.-C. Song, D.-Y. Jeong, and J. Ryu, Pyroelectric energy conversion and its applications - flexible energy harvesters and sensors, Sensors **19**, 2170 (2019).
[86] C. R. Bowen, J. Taylor, E. Le Boulbar, D. Zabek, and V. Yu. Topolov, A modified figure of merit for pyroelectric energy harvesting, Mater. Lett. **138**, 243 (2015).
[87] E. A. Eliseev and A. N. Morozovska, General approach to the description of the size effect in ferroelectric nanosystems, J. Mater. Sci. **44**, 5149 (2009).
[88] W. P. Geng, Y. Liu, X. J. Meng, L. Bellaiche, J. F. Scott, B. Dkhil, and A. Q. Jiang, Giant negative electrocaloric effect in antiferroelectric La-doped Pb (ZrTi) O_3 thin films near room temperature, Adv. Mater. **27**, 3165 (2015).
[89] R. Pirc. Z. Kutnjak, R. Blinc, and Q. M. Zhang, Electrocaloric effect in relaxor ferroelectrics, J. Appl. Phys. **110**, 074113 (2011).